

Condensation models and boundary conditions for non-equilibrium wet steam flows

Frédéric Blondel*

**EDF R&D, 6 Quai Watier, Chatou*
frederic-f.blondel@edf.fr

Bruno Audebert*

**EDF R&D, 6 Quai Watier, Chatou*
bruno.audebert@edf.fr

Thomas Pasutto*

**EDF R&D, 6 Quai Watier, Chatou*
thomas.pasutto@edf.fr

Mugurel Stanciu*

**EDF R&D, 6 Quai Watier, Chatou*
mugurel.stanciu@edf.fr

Abstract

This paper is dedicated to the physical and numerical modelling of wet steam flows with non-equilibrium condensation in power plant steam turbines. The steam, far from an ideal gas behavior is modelled thanks to real gas thermodynamic laws. The nucleation process is taken into account using two models: a simple two-equation model and the Quadrature Method of Moments. The numerical scheme used to handle the complex thermodynamics is the approximate Riemann solver VFRoe for which a particular attention has been paid regarding the boundary conditions. Shock-tube verification test cases are given to check the good behavior of the scheme and validation cases in nozzles are presented to illustrate the accuracy of the physical model compared with experimental data.

Key words : condensation, nucleation, quadrature method of moments, droplets size distribution, real gas, VFRoe scheme, boundary conditions

Introduction

Global understanding of wet steam flows in power plant turbines is of major concern for turbine manufacturers and electricity producers. They have to tackle important issues such as controlling performances and lifetime duration of machines, evaluating new designs or the risks due to the enlargement of operating ranges, predicting and optimizing the maintenance costs.

However, the accurate description of steam turbine's flows is hard to achieve, as many different physical phenomena have to be taken into account. The flow in the complete turbine is highly unsteady due to the blades rotation, tridimensional effects are strong because of the geometrical complexity of the machine and the turbulence prediction for such unsteady tridimensional flows is still an issue. Moreover, the flow is diphasic: high pressure steam turbines operate in totally wet conditions, whereas condensation appears only in the last four stages of the low pressure one's and the accurate prediction of the nucleation and growth processes including droplet size distribution is difficult. In the past, turbine's designers did not take wetness into account during the conception, or they only considered thermodynamic equilibrium conditions between the two phases, which may lead to strong inaccuracies in the prediction of the flow. Yet, a rough estimation of wetness losses represents about five percent of the electrical production since one percent of humidity increases losses by one percent [Baumann 21]. Moreover, the droplets that are created during the pressure expansion along the machine are responsible for turbine blade erosion in the last stages of the low-pressure turbines.

As many efforts are made to solve the issues related to unsteadiness, tridimensional effects and turbulence prediction, wetness prediction is less regarded. Yet, when considering wetness, one has to overcome both modelling and numerical issues.

Concerning modelling issues, steam behaves far from an ideal gas and considering real gas thermodynamic laws is mandatory. Whereas thermodynamic equilibrium models could be sufficient for high pressure turbines, one has to take into account non-equilibrium models because of a delay in the condensation process for low pressure turbines. In these turbines, the droplet size distribution is also of major interest and the modelling of the nucleation is important. For this purpose, mono-dispersed models are the most simple and the most used models [Gerber 04]; [Statsny 08]; [Dykas 12]. Some efforts have been done to use more advanced models, such as the method of moments [White 00]; [Halama 10]; [Chandler 12]. Recently, the Quadrature Method of Moments (QMOM) has been applied to wet steam flows in nozzles [Gerber 07]. In this method, some representative radii are computed and used to model the growth of the liquid phase, so that the flow can be considered as a really poly-dispersed one. This model is a good compromise between simple models and more advanced models such as the method of classes [Kim 89] and it will be considered in this paper.

Concerning numerical issues, the real gas thermodynamics for compressible flows requires the use of adapted numerical schemes. The most natural way to numerically handle such flows is to use the Godunov scheme [Godunov 59] but it requires the resolution of the exact Riemann problem with real gas thermodynamics at each interface, which may be difficult. Approximate Riemann solvers can also be used

such as the well known Roe scheme [Roe 81] which needs an adaptation to real gas [Glaister 88] or more recent schemes that have been designed for this purpose such as relaxation schemes [Coquel 98] or [Coquel 12]. In this paper we have chosen another approximate Riemann solver, the VFRoe scheme [Gallouët 96], [Buffard 00], which is well suited for real gas flows and does not need any adaptation to handle this complex thermodynamics.

Eventually, whatever the scheme one may use to deal with real gas flows, the boundary conditions remain an issue. Inspired by the work of Dubois [Dubois 87], we propose to treat them with a Godunov flux and the exact resolution of half Riemann problems.

In the following, we first address non-equilibrium models and the real gas equation of state of interest for wet steam flows in turbines. After a brief description of the VFRoe scheme, we focus then on the way we handle boundary conditions for wet steam flows. Finally, four verification shock-tube test cases are presented in order to assess the scheme; three validation cases in nozzles deal with the accuracy of the models when comparing them with experimental data.

1 Condensation model

1.1 Equilibrium models

The most simple mono-pressure model that takes condensation into account is based on Euler equations closed with an equilibrium equation of state:

$$\begin{cases} \frac{\partial \rho_m}{\partial t} + \frac{\partial \rho_m u_{m,j}}{\partial x_j} = 0 \\ \frac{\partial \rho_m u_{m,i}}{\partial t} + \frac{\partial (\rho_m u_{m,j} u_{m,i})}{\partial x_j} + \frac{\partial p}{\partial x_i} = 0 \\ \frac{\partial \rho_m E_m}{\partial t} + \frac{\partial \rho_m u_{m,j} H_m}{\partial x_j} = 0 \end{cases} \quad (1)$$

Phase change and liquid phase do not appear explicitly in those equations, but are included in the mixture thermodynamic properties: p the mixture pressure, ρ_m the mixture (m) density, $\mathbf{u}_m = \{u_{m,k}\}_{k=1..3}$ the mixture velocity, E_m the mixture total energy and H_m the mixture total enthalpy. The static temperature is the one of the gaseous phase, and is considered to be the saturation temperature if the saturation line is crossed (the boundary between the gaseous and the mixed gaseous (g) / liquid (l) phases in the Mollier diagram, Fig. 2). Some relations are required to link the gaseous / liquid phase properties with the mixture properties, using the liquid mass fraction y :

$$\left\{ \begin{array}{l} \frac{1}{\rho_m} = \frac{1-y}{\rho_g} + \frac{y}{\rho_l} \\ e_m = (1-y)e_g + ye_l, \\ h_m = (1-y)h_g + yh_l, \\ H_m = h_m + \frac{u_m^2}{2} = (1-y)h_g + yh_l + \frac{u_m^2}{2}, \\ E_m = e_m + \frac{u_m^2}{2} = (1-y)e_g + ye_l + \frac{u_m^2}{2}, \end{array} \right. \quad (2)$$

with e_m the internal energy and $h_m = e_m + p/\rho_m$ the specific enthalpy of the mixture. Equations of state, similar to the one introduced in section 2 can be used to close the problem. It gives the properties of the mixture as a function of the pressure and enthalpy or the pressure and entropy of the mixture. The liquid mass fraction itself is given by the following relation at a given mixture static enthalpy h_m :

$$y(p, h_m) = 1 - \frac{h_m - h_l(p, T_{sat}(p))}{h_g(p, s_g(p, T_{sat}(p))) - h_l(p, T_{sat}(p))}, \text{ if } h_l < h_m < h_g. \quad (3)$$

Relation (3) is also valid using the entropy instead of enthalpy.

1.2 Non-equilibrium models

The condensation in steam turbines (or in supersonic nozzles) occurs at non-equilibrium conditions: as the saturation line is crossed, the flow is still dry (relation (3) is not valid anymore). In this non-equilibrium state, the flow is said to be sub-cooled (the gas phase temperature is below the saturation temperature), until it reaches the Wilson point (the point where the nucleation appears). The position of this point, in terms of pressure and temperature, cannot be easily predicted, as it depends on many parameters, such as the pressure of the flow and the expansion rate. Then, a nucleation shock appears, and a fog of many small droplets is created. The phase change induces a latent heat release, so that the flow comes back to the equilibrium conditions. Neglecting this non-equilibrium process is a strong assumption, as many losses appear when this phenomenon occurs (the entropy increases during the latent heat release). In the sequel, we study two class of non-equilibrium models, namely the simple non-equilibrium model and the quadrature method of moments. For those models, an equation of state adapted to metastable steam conditions is mandatory (see section 2).

1.2.1 A simple non-equilibrium model

Widely applied models for turbomachinery calculations are the mono-dispersed models, where droplets are assumed to have the same mean radius, thus neglecting the size distribution, which is reduced to a function of one radius only. Using the assumptions of an homogeneous flow of non-viscous steam, two equations are added to the previously introduced Euler equation system (1):

$$\begin{cases} \frac{\partial \rho_m y}{\partial t} + \frac{\partial \rho_m u_{m,j} y}{\partial x_j} = \rho_m (N \dot{m}_l + m_l J_{CL}), \\ \frac{\partial \rho_m N}{\partial t} + \frac{\partial \rho_m u_{m,j} N}{\partial x_j} = \rho_m J_{CL}. \end{cases} \quad (4)$$

The first equation in (4) represents the mass conservation of the liquid phase, and the second one represents the conservation of the droplet number. On the right hand side of the first equation, N is the number of droplets per unit mass, \dot{m}_l is the creation of mass due to the growth of the droplets, m_l is the mass of the liquid phase, and J_{CL} is the nucleation rate, given by the classical nucleation theory (see [Bakhtar 05] for a review). Homogeneous models are derived from two-phase inhomogeneous single pressure models by summing the equation sets for the gas and the liquid phase, using a no-slip condition between both phases. As a consequence, there are no source terms on the first three equations (1). The last equation, dedicated to the creation of droplets, is specific to nucleation models. Relations (2) are used to calculate the mixture properties from the gas and liquid phase properties. The source terms involved in the equation for the liquid phase can be written:

$$\begin{cases} \rho_m J_{CL} = \frac{1}{1 + \eta} \sqrt{\frac{2\sigma(T_g)}{\pi m_*^3}} \frac{\rho_m^2}{\rho_l(p)} \exp\left(-\frac{4\pi r_*^2 \sigma(T_g)}{3k_B T_g}\right), \\ \rho_m (N \dot{m}_l + m_l J_{CL}) = \rho_m \frac{4}{3} \pi \rho_l(p) \left(r_*^3 J_{CL} + 3\rho_g N r_{32}^2 \frac{dr}{dt}(r_{32}) \right). \end{cases}$$

Those source terms depend on many parameters defined below. The non-isothermal correction factor η introduced by Kantrowitz [Kantrowitz 51] is written :

$$\eta = \frac{2(\gamma(p, T_g) - 1)}{\gamma(p, T_g) + 1} \frac{L_h(p, T_g)}{R_{H_2O} T_g} \left(\frac{L_h(p, T_g)}{R_{H_2O} T_g} - 0.5 \right), \quad (5)$$

with $\gamma(p, T_g) = c_p(p, T_g)/c_v(p, T_g)$ the ratio of the heat capacities. The critical radius size, which is the minimal radius to ensure the stability of the droplets in the flow:

$$r_* = \frac{2\sigma(T_g)}{\rho_l(p) R_{H_2O} T_g \ln\left(\frac{p}{p_{sat}(T_g)}\right)}, \quad (6)$$

with R_{H_2O} the specific constant of water ($462 J/kg/K$). The mass of a single vapor molecule is:

$$m_* = \frac{M_{H_2O}}{\mathcal{N}_a}, \quad (7)$$

M_{H_2O} being the molar mass of water, and \mathcal{N}_a the Avogadro number ($\mathcal{N}_a \approx 6.022 \times 10^{23} \text{mol}^{-1}$). A good approximation for the surface tension is given by Lamanna

[Lamanna 00]:

$$\sigma(T_g) = \begin{cases} T_g < 250K : \\ 8.52 \times 10^{-2} - 3.54236T_g \times 10^{-4} + 3.50835T_g^2 \times 10^{-6} - 8.71691T_g^3 \times 10^{-9}, \\ T_g \geq 250K : \\ (76.1 + 0.155 \times (273.15 - T_g)) \times 10^{-3}. \end{cases}$$

An expression for the growth of a droplet of radius r , that is suitable whatever the flow regime (defined by the Knudsen number), has been given by Young [Young 82], based on Gyarmathy's law [Gyarmathy 62]:

$$\frac{dr}{dt}(r) = g(r) = \frac{\lambda_g(p, \tau_g)(1 - r_*/r)(T_{sat}(p) - T_g)}{\rho_l(p)L_h(p, T_g)r \left(\frac{1}{1 + 2\beta K_n} + 3.78(1 - \kappa_c)\frac{K_n}{Pr} \right)}. \quad (8)$$

In this expression, $\lambda_g(T_g, \tau_g)$ is the thermal conductivity of the gas phase, $\tau_g = \rho_g^{-1}$ the specific volume, $L_h(p, T_g) = h_g(p, T_g) - h_l(p, T_{sat}(p))$ the latent heat release and $\rho_l(p, T_{sat}(p)) = \rho_l(p)$ the density of the liquid phase (all laws being given by the equation of state), with Knudsen and Prandtl numbers defined as follows, using $\mu_g(T_g, \tau_g)$ the dynamical viscosity of the gas phase and $c_p(p, T_g)$ the heat capacity of the gas phase also given by the equation of state:

$$\begin{cases} K_n = \frac{1.5\mu_g(T_g, \tau_g)\sqrt{R_{H_2O}T_g}}{2r \times p}, \\ Pr = \frac{\mu_g(T_g, \tau_g)c_p(p, T_g)}{\lambda_g(T_g, \tau_g)}. \end{cases}$$

The saturation pressure at a given temperature ($p_{sat}(T_g)$) and the saturation temperature at a given pressure ($T_{sat}(p)$) are also given by the equation of state. The correction factor, κ_c , is usually set to 0 for low-pressure calculations. k_B is the Boltzmann constant ($k_B \approx 1.381e^{-23} J/K$). Eventually, with some abuse in the notations (see section 1.2.2), r_{32} is the mean radius, defined as:

$$r_{32} = \left(\frac{3}{4\pi\rho_l(p)} \frac{y}{N} \right)^{1/3}. \quad (9)$$

1.2.2 Advanced non-equilibrium model: Quadrature Method of Moments

The major drawback of the model introduced in 1.2.1 is that it does not take polydispersion into account: a single average radius is computed. However, the calculation of the global droplet spectra is not yet affordable for industrial calculations. The method of moments is a good alternative to either simple models, such as the two-equation models, or more advanced methods, such as the method of classes [Kim 89], that are often very expensive. The main idea in the method of moments is to

evaluate the lower-order moments of the particle size distribution (PSD). Including nucleation and using the same notation for the growth law of the droplets $g(r)$, the transport equation for the PSD $f(r)$ can be written (see [McGraw 97] for example):

$$\frac{\partial(\rho_m f(r))}{\partial t} + \frac{\partial(\rho_m u_j f(r))}{\partial x_j} + \frac{\partial(\rho_m f(r)g(r))}{\partial r} = \rho_m J_{CL} \delta_{r-r_*}, \quad (10)$$

with J_{CL} the nucleation rate and r_* the critical radius given by (6). The PSD, that is unknown, is now represented by its k -order moments. The moment μ_k of the PSD is written:

$$\mu_k = \int_0^\infty r^k f(r) dr. \quad (11)$$

The lower order moments have a physical meaning, and are used to compute the average droplet radius, the liquid mass fraction and the total number of droplets:

$$r_{32} = \frac{\mu_3}{\mu_2}, \quad y = \frac{4}{3} \pi \rho_l \mu_3, \quad N = \mu_0. \quad (12)$$

Note that the definition of radius r_{32} is not strictly the same between the two-equation model and the method of moments (see equation (9)). With some abuse in the notation, the mean radius is still noted r_{32} for the two-equation model. Using (10) and (11), the transport equation for the moments of the PSD is written:

$$\frac{\partial(\rho_m \mu_k)}{\partial t} + \frac{\partial(\rho_m u_j \mu_k)}{\partial x_j} = \rho_m k \int_0^\infty r^{k-1} g(r) f(r) dr + \rho_m J_{CL} r_*^k. \quad (13)$$

The integral on the right hand side must be evaluated but the distribution function is unknown. The difference between all the existing methods of moments relies on the way this integral is evaluated. We focus here on one particular method, that is the Quadrature Method of Moments (QMOM) proposed by McGraw [McGraw 97]. The QMOM method is widely used (mostly in aerosol sciences) and has been studied in detail [John 12]. This method is very accurate to represent processes such as nucleation and growth but also coagulation, aggregation and breakage (see [Marchisio 03b] for example).

Back to equation (11), McGraw proposed to use a n -point quadrature in order to estimate the moments of the PSD. Using this n -point quadrature, the moments are now written as a sum of radii $\{r_i\}_{i=1..n}$ and weights $\{w_i\}_{i=1..n}$:

$$\mu_k = \sum_{i=1}^n r_i^{k-1} w_i, \quad k \geq 1, \quad (14)$$

The integral in (13) is then approximated by:

$$k \int_0^\infty r^{k-1} g(r) f(r) dr \approx k \sum_{i=1}^n r_i^{k-1} g(r_i) w_i, \quad (15)$$

supposing that $f(r) \approx \sum_{i=1}^n w_i \delta_{r-r_i}$. Using (15), the transport equation (13) is now written:

$$\frac{\partial(\rho_m \mu_k)}{\partial t} + \frac{\partial(\rho_m u_m \mu_k)}{\partial x_j} = \rho_m k \sum_{i=1}^n r_i^{k-1} g(r_i) w_i + \rho_m J_{CL} r_*^k. \quad (16)$$

Then, any law can be used to evaluate the growth of the liquid phase. In practice, we use the law (8) to evaluate $g(r_i)$ for each radius r_i . In order to close the QMOM model, one has to evaluate the weight $\{w_i\}_{i=1..n}$ and the radii $\{r_i\}_{i=1..n}$. This is done with a quadrature algorithm. The accuracy of the method clearly depends on the accuracy of this algorithm. In our study, the Wheeler algorithm has been used (see [Press 92] and [John 12]). With this algorithm, the number of computed radii is $n = k/2$ when using k moments. In our calculations, we have computed 12 moments and thus 6 radii, otherwise the quadrature algorithm may fail and lead to non-physical radii because the computed value of higher moments is too close to round-off errors. Moreover, the evaluation of the weights and radii requires that the moments of the PSD are non-zero which is not the case when nucleation occurs since the flow is dry before the creation of the droplets. In order to overcome this issue, some authors proposed to add seeds at the inlet of the computational domain [Marchisio 05]. In our case, this was not necessary; using a non-zero distribution at the initialization was sufficient to take nucleation into account.

Remark 1 (Hyperbolicity) Providing that the square of the sound velocity remains positive, the global system composed of the Euler system with q transported equations is hyperbolic ((1) with (4) or (16)), as supplementary equations are convected scalars only, with zero-order source terms. The positivity of the square of the sound velocity is ensured by the thermodynamic formulation, as long as the polynomial expressions are used in their definition domain (see the following section 2).

2 Non-equilibrium wet steam Equation of State

As previously mentioned, condensation in steam turbines (or supersonic nozzles) occurs at non-equilibrium thermodynamic conditions: a fog of small droplets appears as the static temperature is far below the saturation line. Thus, a specific equation of state has to be used. The IAPWS-IF97 provides this kind of formulation, and is now recognized as one of the most accurate for industrial applications [IAPWS 07]. Steam properties are given in the form of 13th order polynomial expressions for dry steam and metastable (or sub-cooled) steam. A similar formulation is given for equilibrium condensation (see section 1), but only the dry and metastable formulations are of interest here, dealing with non-equilibrium condensation. Also, similar expressions are given for the liquid phase properties (such as the density, enthalpy, entropy...). Thus, properties of the mixture required to close system (1) can be computed using both the liquid mass fraction, given by the condensation model, and the polynomial expressions for the gaseous and the liquid phase, using relations (2).

The general form of those polynomial expressions is the following:

$$\frac{\mathcal{G}(p, T)}{RT} = \gamma(\pi, \xi) = \gamma^0(\pi, \xi) + \gamma^r(\pi, \xi), \quad (17)$$

with \mathcal{G} the specific Gibbs free energy, p the pressure, T the gas temperature (for the sake of simplicity, we do not keep here the notation T_g of the previous section), π the reduced pressure $\pi = (p/p^*)$ and ξ the inverse reduced temperature $\xi = (T^*/T)$, p^* and T^* being given constants (equal to 1 MPa and 540 K respectively). In this equation, γ^0 represents the ideal-gas part and γ^r the residual part. In the stable (or dry) region, the residual part is given as 43th order polynomial whereas in the metastable part, it is given as 13th order polynomial expressions. The ideal-gas part can be written:

$$\gamma^0 = \ln(\pi) + \sum_{i=1}^9 n_i^0 \xi^{J_i^0}, \quad (18)$$

where n_i^0 , J_i^0 are given constants, and the residual part:

$$\gamma^r = \sum_{i=1}^{13} n_i \pi^{I_i} (\xi - 0.5)^{J_i}, \quad (19)$$

with n_i , I_i , J_i the remaining constant coefficients of the model. Details of this formulation and constant values can be found in [IAPWS 07]. The domain of validity of this equation of state is also given in [IAPWS 07] and is reproduced here (Fig. 1) where the domain is divided in 5 regions. Each region has specific constants for the polynomial expressions. The curve noted 4 is the saturation curve. Regions 1 and 3 are the liquid regions whereas regions 2 and 5 are the vapor regions. Region 5 is specific for high temperature gas and is not relevant for steam turbines. The metastable region which is of particular interest for non-equilibrium wet steam is located in region 1 near the saturation curve. It comes from an extrapolation of the polynomial functions of region 2.

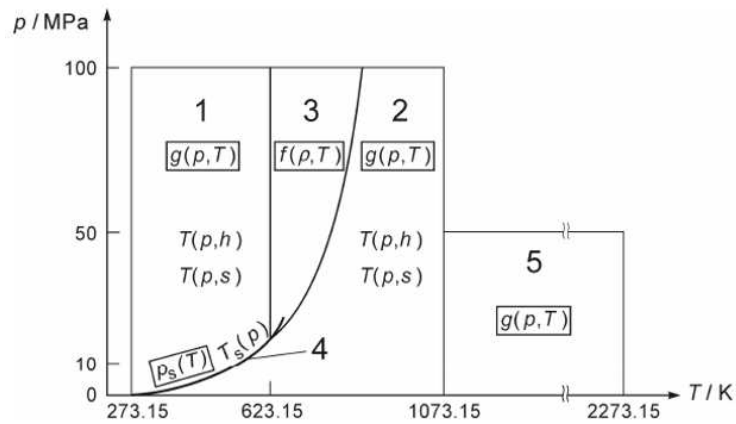


Figure 1: Region of validity for IAPWS-IF97

At this point, the calculation of the static gas temperature T as a function of the other variables is not yet resolved. To avoid the inversion of the polynomial expressions (which have a high computational cost when extensively used), some "backward expressions" have been derived for static temperature as a function of pressure and specific enthalpy or entropy. Those backward expressions can then be used to express any thermodynamic properties as a function of the pressure and the temperature, the temperature being a function of pressure and enthalpy or entropy.

Then, thermodynamic properties, such as the specific volume τ , the internal energy e , the specific enthalpy h , the isobaric and the isochoric heat capacities c_p and c_v , and the speed of sound c have to be expressed as functions of the specific Gibbs free energy \mathcal{G} :

$$\begin{aligned}\tau &= (\partial\mathcal{G}/\partial p)_T, \\ e &= \mathcal{G} - T(\partial\mathcal{G}/\partial T)_p - p(\partial\mathcal{G}/\partial p)_T, \\ s &= -(\partial\mathcal{G}/\partial T)_p, \\ h &= \mathcal{G} - T(\partial\mathcal{G}/\partial T)_p, \\ c_p &= (\partial h/\partial T)_p, \\ c_v &= (\partial e/\partial T)_\tau, \\ c &= \tau(-(\partial p/\partial \tau)_s)^{1/2}.\end{aligned}$$

Finally, each thermodynamic property is given as a function of pressure and enthalpy (or entropy), temperature being itself a function of pressure and enthalpy (or entropy). With some abuse in the notations, relations read:

$$\begin{array}{ll}\tau = \tau(p, h), & \tau = \tau(p, s), \\ e = e(p, h), & e = e(p, s), \\ s = s(p, h), & \text{or} \quad h = h(p, s), \\ c^2 = c^2(p, h), & c^2 = c^2(p, s), \\ T = T(p, h). & T = T(p, s).\end{array}$$

The dynamical viscosity $\mu(T, \tau)$ (respectively the thermal conductivity $\lambda(T, \tau)$) is calculated thanks to an IAPWS-2008 [IAPWS 08] formulation (respectively an IAPWS-2011 [IAPWS 11] formulation) with $T(p, s)$ or $T(p, h)$ and $\tau(p, s)$ or $\tau(p, h)$ previously defined for IAPWS-IF97. These two formulations are not detailed here, but they are compatible with the IAPWS-IF97 formulation. Finally, properties of the liquid phase are calculated in a very similar way, though the coefficients of the polynomial expressions have to be adapted.

As many polynomial expressions with high orders are used, the computational cost for this kind of equation of state is very high, that is to say almost prohibitive, when used in CFD codes. That is why those expressions have been tabulated. The use of tables greatly reduces the computational cost of a scheme, which is then very close to the cost when using an ideal-gas equation of state. It has been checked that the computational cost is increased by one to two orders of magnitude when using polynomial expressions. The pressure and the temperature ranges encountered in steam

turbines being wide, interpolations in a thermodynamic table may be performed using splines and also a logarithmic scale can be used in order to have the finest resolution close to the saturation line and near vacuum. With the one-dimensional nozzle code used in this paper, simple constant step tables have been generated, and thermodynamic properties are stored in 2D tables in order to be directly accessible, knowing the step, the minimal, and the maximal values of the table. A simple bi-linear approximation is then performed between table steps. This methodology leads to very small (that is to say negligible) errors on the thermodynamic expressions (using the computer program verifications given by the IAPWS).

Table 1 shows the relative errors between the polynomial expressions and the values interpolated in the table. For this illustration, three points have been chosen in terms of pressure (5 bar, 2 bar, and 0.25 bar), using three different subcooling degrees (-40 K, 0 K, $+40$ K). The maximal relative error found during the tests is $4\text{E-}6$.

p [bar]:	5	2	0.25	5	2	0.25	5	2	0.25
ΔT [K]:	-40			0			+40		
ρ	3E-7	5E-8	4E-6	5E-8	8E-8	4E-6	3E-7	5E-8	4E-6
h	1E-7	2E-8	5E-10	2E-8	4E-9	5E-10	1E-7	2E-8	5E-10
e	1E-7	1E-8	3E-10	2E-8	4E-9	6E-10	1E-7	1E-8	3E-10
s	1E-7	2E-8	1E-7	3E-8	1E-8	1E-7	1E-7	2E-8	1E-7
c^2	4E-7	1E-7	1E-8	1E-7	2E-8	5E-9	4E-7	1E-7	1E-8

Table 1: Relative errors between tabulated and polynomial EOS

3 VFRoe scheme

3.1 Finite volume formulation of the problem

Considering only the first order underlying system, Euler equations (1) with a condensation model of the form (4) or (16) can be formally written:

$$\frac{\partial \mathbf{w}(\mathbf{x}, t)}{\partial t} + \sum_{k=1}^d \frac{\partial \mathbf{F}_k(\mathbf{w}(\mathbf{x}, t))}{\partial x_k} = 0, \quad (20)$$

with d the space dimension, \mathbf{F}_k the fluxes in the k space direction, and $\mathbf{w} = (\rho, \rho \mathbf{u}, \rho E, \rho \boldsymbol{\psi}) \in \mathbb{R}^{2+d+q}$ the vector of conservative variables where $\{\boldsymbol{\psi}\}_{k=1..q}$ stands for the q transported variables of the condensation model. The computational domain \mathcal{O} is composed of N_c cells (or control volumes) $\{\Omega_i\}_{i=1..N_c}$, on which the solution represented by the conservative variables $\mathbf{w}(\cdot, t)$ is approximated by a constant $\mathbf{w}_i(t)$, representing an approximation of the average value of $\mathbf{w}(\cdot, t)$ on the control volume Ω_i :

$$\mathbf{w}_i(t) \approx \frac{1}{|\Omega_i|} \int_{\Omega_i} \mathbf{w}(\mathbf{x}, t) d\mathbf{x}. \quad (21)$$

The domain boundaries are noted $\partial\mathcal{O}$. Integrating (20) over a control volume Ω_i leads to:

$$\frac{\partial}{\partial t} \left(\int_{\Omega_i} \mathbf{w}(\mathbf{x}, t) d\mathbf{x} \right) + \int_{\partial\Omega_i} \sum_{k=1}^d \mathbf{F}_k(\mathbf{w}(\mathbf{x}, t)) \nu_{i,k} d\sigma = 0. \quad (22)$$

The boundary of Ω_i is $\partial\Omega_i$ and $\nu_{i,k}$ the exterior normal vector to this cell. The first term in (21) is approximated by:

$$\frac{\partial}{\partial t} \left(\int_{\Omega_i} \mathbf{w}(\mathbf{x}, t) d\mathbf{x} \right) \approx |\Omega_i| \frac{\partial \mathbf{w}_i(t)}{\partial t}, \quad (23)$$

and the second term by:

$$\begin{aligned} \int_{\partial\Omega_i} \sum_{k=1}^d \mathbf{F}_k(\mathbf{w}(\mathbf{x}, t)) \nu_{i,k} d\sigma &= \sum_{j \in \mathcal{V}(i)} \int_{\Gamma_{ij}} \sum_{k=1}^d \mathbf{F}_k(\mathbf{w}(\mathbf{x}, t)) \nu_{i,k} d\sigma \\ &+ \sum_{l \in \mathcal{V}_b(i)} \int_{\Gamma_{bil}} \sum_{k=1}^d \mathbf{F}_{b,k}(\mathbf{w}(\mathbf{x}, t)) \nu_{i,k} d\sigma, \end{aligned} \quad (24)$$

where $\mathcal{V}(i)$ are the index subset of the neighboring cells of the control volume Ω_i , and $\mathcal{V}_b(i)$ the index subset of the boundary faces in common with Ω_i faces. Ω_i boundaries are constituted by $\partial\Omega_i = (\cup_j \Gamma_{ij}, \cup_l \Gamma_{bil})$ with $\Gamma_{ij} = \Omega_i \cap \Omega_j$ the inner face between two adjacent cells Ω_i and Ω_j and $\Gamma_{bil} = \Omega_i \cap \partial\mathcal{O}$ the boundary face between the control volume Ω_i and the boundary of the domain $\partial\mathcal{O}$.

A numerical flux has to be defined to approximate $\int_{\Gamma_{ij}} \sum_{k=1}^d \mathbf{F}_k(\mathbf{w}(\mathbf{x}, t)) \nu_{i,k} d\sigma$ and $\int_{\Gamma_{bil}} \sum_{k=1}^d \mathbf{F}_{b,k}(\mathbf{w}(\mathbf{x}, t)) \nu_{i,k} d\sigma$. A numerical two-point flux function, \mathbf{F}^{num} , is introduced, so that one can write for each inner and boundary face (Γ_{ij} and Γ_{bil}):

$$\int_{\Gamma_{ij}} \sum_{k=1}^d \mathbf{F}_k(\mathbf{w}(\mathbf{x}, t)) \nu_{i,k} d\sigma = |\Gamma_{ij}| \sum_{k=1}^d \mathbf{F}_k^{num}(\mathbf{w}_i, \mathbf{w}_j) n_{ij,k}, \quad (25)$$

$$\int_{\Gamma_{bil}} \sum_{k=1}^d \mathbf{F}_{b,k}(\mathbf{w}(\mathbf{x}, t)) \nu_{i,k} d\sigma = |\Gamma_{bil}| \sum_{k=1}^d \mathbf{F}_{b,k}^{num}(\mathbf{w}_i) n_{bil,k}, \quad (26)$$

with \mathbf{n}_{ij} the normal unitary vector getting out the inner face Γ_{ij} and \mathbf{n}_{bil} the normal unitary vector getting out the boundary face Γ_{bil} .

The finite volume discretization of this equation with a two-point numerical flux inside the computational domain leads to the general formulation:

$$|\Omega_i| \frac{\partial \mathbf{w}_i(t)}{\partial t} + \sum_{j \in \mathcal{V}(i)} |\Gamma_{ij}| \sum_{k=1}^d \mathbf{F}_k^{num}(\mathbf{w}_i, \mathbf{w}_j) n_{ij,k} + \sum_{l \in \mathcal{V}_b(i)} |\Gamma_{bil}| \sum_{k=1}^d \mathbf{F}_{b,k}^{num}(\mathbf{w}_i) n_{bil,k} = 0. \quad (27)$$

The time integration has to be achieved. A simple one-step explicit Backward Euler scheme is used:

$$\frac{|\Omega_i|}{\Delta t} (\mathbf{w}_i^{n+1} - \mathbf{w}_i^n) + \sum_{j \in \mathcal{V}(i)} |\Gamma_{ij}| \sum_{k=1}^d \mathbf{F}_k^{num}(\mathbf{w}_i^n, \mathbf{w}_j^n) n_{ij,k} + \sum_{l \in \mathcal{V}_b(i)} |\Gamma_{bil}| \sum_{k=1}^d \mathbf{F}_{b,k}^{num}(\mathbf{w}_i^n) n_{bil,k} = 0. \quad (28)$$

Then, a numerical scheme has to be defined to estimate the numerical flux \mathbf{F}_k^{num} . Next section introduces the VFRoe scheme for the inner faces. The flux used for the boundary faces will be introduced in section 4.

3.2 Principle of the VFRoe scheme for inner fluxes

We first introduce the exact normal flux associated with system (20):

$$\mathcal{F}(\mathbf{w}(\mathbf{x}, t); \mathbf{n}) = \sum_{k=1}^d \mathbf{F}_k(\mathbf{w}(\mathbf{x}, t))n_k, \quad (29)$$

and the numerical two-point normal flux to the inner faces:

$$\mathcal{F}_{ij}^{num}(\mathbf{w}_i, \mathbf{w}_j; \mathbf{n}_{ij}) = \sum_{k=1}^d \mathbf{F}_k^{num}(\mathbf{w}_i, \mathbf{w}_j)n_{ij,k}. \quad (30)$$

For the Euler equations with q transported variables $\boldsymbol{\psi} = \{\psi_k\}_{k=1..q}$, the exact normal flux is:

$$\mathcal{F}(\mathbf{w}(\mathbf{x}, t); \mathbf{n}) = \begin{pmatrix} \rho(\mathbf{u} \cdot \mathbf{n}) \\ \rho(\mathbf{u} \cdot \mathbf{n})\mathbf{u} + p\mathbf{n} \\ (\rho E + p)(\mathbf{u} \cdot \mathbf{n}) \\ \rho\boldsymbol{\psi} \cdot \mathbf{n} \end{pmatrix}. \quad (31)$$

We now define the system written in the normal $\mathbf{n} = \mathbf{n}_{ij}$ direction of each inner face of the mesh which will be useful to define the Riemann problem of interest for the VFRoe scheme. Invoking the invariance of the Euler equations under frame rotation, system (20) can be easily written in the local frame $(\mathbf{n}, \boldsymbol{\tau}_1, \boldsymbol{\tau}_2)$ associated with each inner face, where $\boldsymbol{\tau}_1$ and $\boldsymbol{\tau}_2$ are two tangential vectors constituting a basis of \mathbb{R}^3 with the normal \mathbf{n} . Neglecting the transverse variations of \mathbf{w} with respect to $\boldsymbol{\tau}_1$ and $\boldsymbol{\tau}_2$, the normal system associated with (20) is:

$$\begin{cases} \partial_t \rho + \partial_n(\rho u_n) = 0, \\ \partial_t(\rho u_n) + \partial_n(\rho u_n^2 + p) = 0, \\ \partial_t(\rho E) + \partial_n(u_n(\rho E + p)) = 0, \\ \partial_t(\rho\boldsymbol{\psi}) + \partial_n(\rho u_n\boldsymbol{\psi}) = 0, \\ \partial_t(\rho u_{\boldsymbol{\tau}_1}) + \partial_n(\rho u_n u_{\boldsymbol{\tau}_1}) = 0, \\ \partial_t(\rho u_{\boldsymbol{\tau}_2}) + \partial_n(\rho u_n u_{\boldsymbol{\tau}_2}) = 0, \end{cases} \quad (32)$$

where $u_n = \mathbf{u} \cdot \mathbf{n}$ is the normal velocity and $u_{\boldsymbol{\tau}_{1,2}} = \mathbf{u} \cdot \boldsymbol{\tau}_{1,2}$ are the transverse velocities.

The VFRoe scheme is a Godunov-type scheme [Godunov 59] similar to the Roe scheme [Roe 81]. It is based on the resolution of an approximate Riemann problem at each inner face of the mesh. Unlike the Roe scheme, it does not require to respect a Roe condition to be conservative [Gallouët 96], [Masella 99]. Several VFRoe schemes can be defined depending on the variable used to calculate the solution of the Riemann problem at each inner face between two adjacent cells of the mesh. The natural choice is based on the conservative variable \mathbf{w} but other choices can be

made as soon as the change of variable is admissible (when the chosen variable is not the conservative one, the scheme is called VFRoency [Buffard 00], but we will always keep the name VFRoe scheme in this paper). However this choice will have some consequences on the properties of the scheme [Gallouët 03]. The principle of this scheme is the following:

Principle of the VFRoe scheme

If $\mathbf{Y}(\mathbf{w})$ is an admissible change of variable, the VFRoe flux is written:

$$\mathcal{F}^{\text{VFRoe}}(\mathbf{w}_i; \mathbf{w}_j; \mathbf{n}_{ij}) = \mathcal{F}(\mathbf{w}(\mathbf{Y}_{ij}^*); \mathbf{n}_{ij}), \quad (33)$$

with \mathbf{Y}_{ij}^* the solution of the linearized Riemann problem at each inner face of the mesh separating constant left and right states \mathbf{w}_i and \mathbf{w}_j of the cells Ω_i and Ω_j , and associated with the system (32) written in the normal direction \mathbf{n}_{ij} to this face. Choices have to be done to fully define the numerical flux:

- Choice of the \mathbf{Y} variable.
- Choice of the linearization.

We detail below the specific choice $(s, u_n, p, \boldsymbol{\psi})$ for the \mathbf{Y} variable.

3.3 VFRoe scheme using $(s, u_n, p, \boldsymbol{\psi})$ variables

From now on, the transported tangential velocities are considered as a part of the vector $\boldsymbol{\psi}$. As we mentioned in the previous section, the choice of the variable \mathbf{Y} may have an influence on the scheme properties. Some propositions have already been given in the literature [Buffard 00], [Gallouët 03]:

- $\mathbf{Y} = \mathbf{w}$, the conservative variable,
- $\mathbf{Y} = (1/\rho, u_n, p, \boldsymbol{\psi})$,
- $\mathbf{Y} = (s, u_n, p, \boldsymbol{\psi})$.

Choosing primitive variables $(., u_n, p, \boldsymbol{\psi})$ is a natural choice to keep the contact discontinuity unmodified during the resolution of the linearized Riemann problem (*i.e.* u and p are kept constant through the contact discontinuity during this resolution). Then, the choice of $1/\rho$ as a first component of \mathbf{Y} is only useful when considering ideal gas law, as in this particular case the approximate jump relations used for the resolution of the linearized Riemann problem are equivalent to the exact ones [Buffard 00]. As this paper deals with real gas, this choice is not interesting. Choosing the entropy as the first component of \mathbf{Y} leads to a better accuracy when thermodynamic conditions are close to vacuum. Under some conditions [Gallouët 03], positivity of ρ and p may be kept for the linearized Riemann problem. In steam turbines used in the secondary loop of nuclear power plant, the pressure beyond

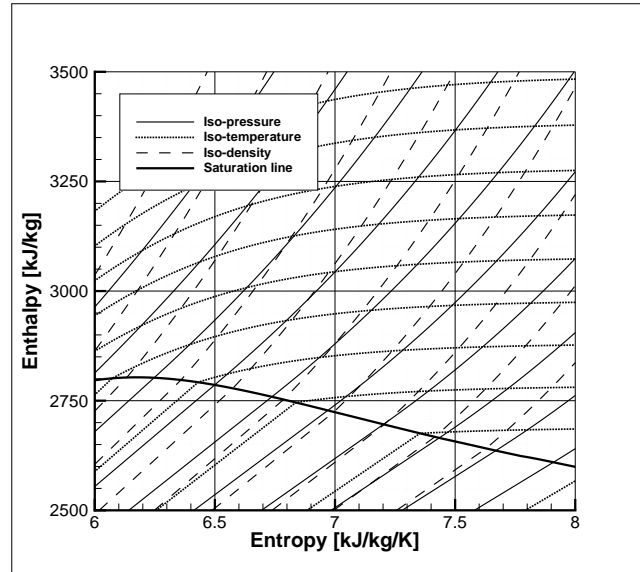


Figure 2: H-S Mollier diagram

the last stage of the turbine is very low (a few millibars) so that dealing with near vacuum conditions in this kind of application is of particular interest. A physical argument could also be invoked to justify the choice of s . Using $(1/\rho, u_n, p, \psi)$, all the thermodynamic quantities such as the internal energy must be evaluated from the pressure and the density by $e = e(p, 1/\rho)$. Using the second set of variables (s, u_n, p, ψ) , thermodynamic quantities have to be evaluated from pressure and entropy ($\tau = \tau(p, s)$ and $e = e(p, s)$ for example). In the Mollier diagram (see Fig. 2) which defines the thermodynamic law used for steam, iso-pressure and iso-density curves are very close from each other and almost parallel, so that a small error on pressure would lead to a large error on density, and the error committed on the evaluation of $e(p, 1/\rho)$ or on another thermodynamic quantity would be very high. Iso-pressure and iso-entropy curves are much more independent quantities, and the error during the evaluation of thermodynamic quantities ($\tau(p, s)$ or $e(p, s)$ for instance) will be smaller.

Thus, the chosen set for the primitive variable is:

$$\mathbf{Y} = (s, u_n, p, \psi) \quad (34)$$

3.3.1 Linearized Riemann problem

For the sake of simplicity, we consider that the vector ψ is now of dimension one, so that it is only a scalar noted ψ but the generalization of the following to q transported variables is straightforward. The mono-dimensional system (32) can be written under the following linearized form:

$$\partial_t \mathbf{Y} + B(\hat{\mathbf{Y}}) \partial_n \mathbf{Y} = 0 \quad (35)$$

using " $\widehat{\cdot}$ " as a linearization. This system has the explicit classical following form:

$$\begin{cases} \partial_t s + \widehat{u}_n \partial_n s = 0, \\ \partial_t u_n + \widehat{u}_n \partial_n u_n + \widehat{\tau(p, s)} \partial_n p = 0, \\ \partial_t p + \widehat{u}_n \partial_n p + \frac{\widehat{c^2}}{\tau} (p, s) \partial_n u_n = 0, \\ \partial_t \psi + \widehat{u}_n \partial_n \psi = 0, \end{cases} \quad (36)$$

with $\tau = \rho^{-1}$ the specific volume. The Jacobian matrix $B(\widehat{\mathbf{Y}})$ is then given by:

$$B(\widehat{\mathbf{Y}}) = \begin{pmatrix} \widehat{u}_n & 0 & 0 & 0 \\ 0 & \widehat{u}_n & \widehat{\tau} & 0 \\ 0 & \frac{\widehat{c^2}}{\tau} & \widehat{u}_n & 0 \\ 0 & 0 & 0 & \widehat{u}_n \end{pmatrix}.$$

3.3.2 Choice of the linearization procedure

A classical choice is done, noting $\bar{\mathbf{X}} = \frac{1}{2}(\mathbf{X}_i + \mathbf{X}_j)$ for all \mathbf{X} except τ and c^2 . In this paper, we have chosen:

$$\begin{cases} \widehat{\tau(p, s)} = \tau(\bar{p}, \bar{s}), \\ \frac{\widehat{c^2}}{\tau}(p, s) = \frac{c^2(\bar{p}, \bar{s})}{\tau(\bar{p}, \bar{s})}. \end{cases}$$

Using abusive notations, we will note afterwards $\bar{\tau} \equiv \tau(\bar{p}, \bar{s})$ and $\bar{c}^2 \equiv c^2(\bar{p}, \bar{s})$.

3.3.3 Resolution of the linearized Riemann problem

We consider here the Riemann problem associated with the linearized system (36) centered at the inner face Γ_{ij} between two adjacent cells Ω_i and Ω_j and in the normal direction \mathbf{n}_{ij} to this inner face, completed with the initial condition ($\mathbf{Y}_l = \mathbf{Y}_i, \mathbf{Y}_r = \mathbf{Y}_j$).

For such a linearized Riemann problem (LRP) there is an existing representation formula: the LRP associated with (36) is made of four states ($\mathbf{Y}_l = \mathbf{Y}_i; \mathbf{Y}_1; \mathbf{Y}_2; \mathbf{Y}_r = \mathbf{Y}_j$) separated by at most three simple waves (with some abuse in the notation, x stands for the coordinate along the normal to the inner face, with $x = 0$ at the inner face):

$$\mathbf{Y} \left(\frac{x}{t}; \mathbf{Y}_l, \mathbf{Y}_r \right) = \mathbf{Y}_l + \sum_{\frac{x}{t} > \lambda_k} {}^t \mathbf{l}_k (\mathbf{Y}_r - \mathbf{Y}_l) \mathbf{r}_k = \mathbf{Y}_r - \sum_{\frac{x}{t} \leq \lambda_k} {}^t \mathbf{l}_k (\mathbf{Y}_r - \mathbf{Y}_l) \mathbf{r}_k, \quad (37)$$

with $\{\mathbf{l}_k\}_{k=1..4}$ and $\{\mathbf{r}_k\}_{k=1..4}$ the left and right eigenvectors of $B(\bar{\mathbf{Y}})$ and $\{\lambda_k\}_{k=1..4}$ its eigenvalues given by:

$$\lambda_1 = \bar{u}_n - \bar{c}; \quad \lambda_2 = \bar{u}_n; \quad \lambda_3 = \bar{u}_n; \quad \lambda_4 = \bar{u}_n + \bar{c}; \quad \text{with } \bar{c} \equiv \sqrt{(\bar{c}^2)},$$

$$\mathbf{r}_1 = \begin{pmatrix} 0 \\ \bar{\tau} \\ -\bar{c} \\ 0 \end{pmatrix}; \quad \mathbf{r}_2 = \begin{pmatrix} 1 \\ 0 \\ 0 \\ 0 \end{pmatrix}; \quad \mathbf{r}_3 = \begin{pmatrix} 0 \\ 0 \\ 0 \\ 1 \end{pmatrix}; \quad \mathbf{r}_4 = \begin{pmatrix} 0 \\ \bar{\tau} \\ \bar{c} \\ 0 \end{pmatrix};$$

$$\mathbf{l}_1 = \frac{1}{2\tilde{c}\tilde{\tau}} \begin{pmatrix} 0 \\ \tilde{c} \\ -\tilde{\tau} \\ 0 \end{pmatrix}; \quad \mathbf{l}_2 = \begin{pmatrix} 1 \\ 0 \\ 0 \\ 0 \end{pmatrix}; \quad \mathbf{l}_3 = \begin{pmatrix} 0 \\ 0 \\ 0 \\ 1 \end{pmatrix}; \quad \mathbf{l}_4 = \frac{1}{2\tilde{c}\tilde{\tau}} \begin{pmatrix} 0 \\ \tilde{c} \\ \tilde{\tau} \\ 0 \end{pmatrix}.$$

The solution of the Riemann problem \mathbf{Y}_{ij}^* at the inner faces Γ_{ij} is thus given by:

$$\mathbf{Y}_{ij}^* = \mathbf{Y}(0; \mathbf{Y}_l, \mathbf{Y}_r) = \begin{pmatrix} \mathbf{Y}_l = \mathbf{Y}_i, & \text{if } \lambda_1 > 0 & \Leftrightarrow & \bar{u}_n > \tilde{c} \\ \mathbf{Y}_1, & \text{if } \lambda_1 \leq 0 \text{ and } \lambda_2 > 0 & \Leftrightarrow & 0 < \bar{u}_n \leq \tilde{c} \\ \mathbf{Y}_2, & \text{if } \lambda_2 \leq 0 \text{ and } \lambda_4 > 0 & \Leftrightarrow & -\tilde{c} < \bar{u}_n \leq 0 \\ \mathbf{Y}_r = \mathbf{Y}_j, & \text{if } \lambda_4 \leq 0 & \Leftrightarrow & \bar{u}_n \leq -\tilde{c} \end{pmatrix}. \quad (38)$$

To give an explicit formulation of the intermediate states, we write $\alpha_k = {}^t\mathbf{l}_k(\mathbf{Y}_r - \mathbf{Y}_l) = {}^t\mathbf{l}_k[\mathbf{Y}_l^r]$:

$$\begin{cases} \alpha_1 = \frac{1}{2\tilde{\tau}}[u_n]_l^r - \frac{1}{2\tilde{c}}[p]_l^r, \\ \alpha_2 = [s]_l^r, \\ \alpha_3 = [\psi]_l^r, \\ \alpha_4 = \frac{1}{2\tilde{\tau}}[u_n]_l^r + \frac{1}{2\tilde{c}}[p]_l^r. \end{cases} \quad (39)$$

Finally, intermediate states are given by:

$$\begin{aligned} \mathbf{Y}_1 &= \mathbf{Y}_l + \alpha_1 \mathbf{r}_1 = \begin{pmatrix} s_l \\ (u_n)_l \\ p_l \\ \psi_l \end{pmatrix} + \alpha_1 \begin{pmatrix} 0 \\ \tilde{\tau} \\ -\tilde{c} \\ 0 \end{pmatrix}, \\ \mathbf{Y}_2 &= \mathbf{Y}_r - \alpha_4 \mathbf{r}_4 = \begin{pmatrix} s_r \\ (u_n)_r \\ p_r \\ \psi_r \end{pmatrix} - \alpha_4 \begin{pmatrix} 0 \\ \tilde{\tau} \\ \tilde{c} \\ 0 \end{pmatrix}. \end{aligned} \quad (40)$$

3.4 Entropy correction

As for the Roe scheme, the VFRoe scheme needs an entropy correction to handle correctly the expansion across sonic points, and avoid non-physical shock waves. In the case of supersonic nozzle with condensation, sonic points in an expansion wave may be crossed once to three times: at the throat of the nozzle, and in the condensation shock if the heat release is super-critical (or critical), and after the condensation shock. Thus, the entropy correction is mandatory. In order to detect the sonic points, the following test is performed at each inner face [Helluy 10]:

$$\lambda_k(\mathbf{w}_i)\lambda_k(\mathbf{w}_j) < 0 \text{ and } [u_n]_i^j \geq 0, \quad \text{for } k = 1 \text{ and } k = 4. \quad (41)$$

If this assertion is true, the VFRoe flux is replaced by a modified VFRoe flux:

$$\mathcal{F}_{ij}^{\text{MVFRoe}}(\mathbf{w}_i, \mathbf{w}_j, \mathbf{n}_{ij}) = \mathcal{F}_{ij}^{\text{VFRoe}}(\mathbf{w}_i, \mathbf{w}_j, \mathbf{n}_{ij}) - \frac{\min(|\lambda_k(\mathbf{w}_i)|, |\lambda_k(\mathbf{w}_j)|)}{2} (\mathbf{w}_j - \mathbf{w}_i). \quad (42)$$

Note that this correction does not require any parameter.

4 Boundary Conditions

A numerical flux has to be prescribed at boundary faces $\Gamma_{b_{il}}$. It is not mandatory to give the same numerical flux at the boundary as the inner face flux. Our strategy consists in using a Godunov flux at the boundary [Dubois 87]. As the number of boundary faces is usually far less large than the number of inner faces, the computational cost of such an approach remains affordable. We first define the normal numerical flux at a boundary face $\Gamma_{b_{il}}$ of the cell Ω_i :

$$\mathcal{F}_{b_{il}}^{num}(\mathbf{w}_i; \mathbf{n}_{b_{il}}) = \sum_{k=1}^d \mathbf{F}_{b,k}^{num}(\mathbf{w}_i) n_{b_{il},k}. \quad (43)$$

With this definition, the numerical flux at the boundary is given by:

$$\mathcal{F}_{b_{il}}^{num}(\mathbf{w}_i; \mathbf{n}_{b_{il}}) = \mathcal{F}_{b_{il}}^{God}(\mathbf{w}_i; \mathbf{n}_{b_{il}}) = \mathcal{F}_{b_{il}}(\mathbf{w}(\mathbf{Y}_{b_{il}}^*); \mathbf{n}_{b_{il}}), \quad (44)$$

where $\mathcal{F}(\mathbf{w}; \mathbf{n})$ is the normal flux defined by (29) and $\mathbf{Y}_{b_{il}}^* = (s_{b_{il}}, (u_n)_{b_{il}}, p_{b_{il}}, \psi_{b_{il}})$ is the solution of the *exact* half Riemann problem at the boundary face $\Gamma_{b_{il}}$ between \mathbf{w}_i^n the value of \mathbf{w} in the cell Ω_i and \mathbf{w}^{ext} the prescribed or known value of \mathbf{w} outside the domain \mathcal{O} . We remind that we consider the tangential velocities as a part of the vector $\boldsymbol{\psi}$ and that for the sake of simplicity, the vector $\boldsymbol{\psi}$ is considered as a scalar quantity ψ (the generalization of this section is however straightforward for q transported quantities).

Depending on the type of boundary conditions (inlet, outlet, wall, ...) and thus the number of information given by the user, several *scenarii* have to be performed to calculate the exact half Riemann problem at a given boundary face and to fully prescribe the flux. In this paper, we will focus on two particular boundary conditions and its associated *scenarii*, namely a constant pressure and constant enthalpy subsonic inlet and a supersonic outlet (the case of a constant pressure subsonic outlet is described in the appendix 1 and the case of an adiabatic wall in the appendix 2).

4.1 Constant pressure constant enthalpy subsonic inlet condition

For an inlet boundary condition, the static pressure, the total enthalpy and all transported quantities next to the exterior of the boundary faces are considered to be given by the user. First of all, some thermodynamic relations are needed. The real gas law used for this model gives the following relations (with some abuse in the notations):

$$s = s(p, h), \quad (45)$$

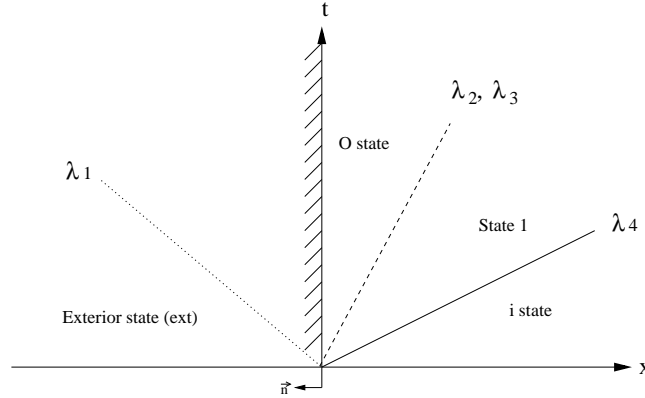
$$\tau = \tau(p, h), \quad (46)$$

$$c^2 = c^2(p, s), \quad (47)$$

$$h = h(p, s), \quad (48)$$

$$\tau = \tau(p, s). \quad (49)$$

In the sequel, the notations are those of the Fig. 3, so that we are looking for the state 0 at the boundary face knowing the whole right state of the half Riemann


 Figure 3: Riemann problem at the inlet, first *scenario*

problem which corresponds to \mathbf{w}_i^n value of \mathbf{w} in the first cell Ω_i of the domain at time t^n .

The *scenario* for this boundary condition is based on the following assumptions:

- The pressure p^{ext} , the total enthalpy H^{ext} and the transported quantity ψ^{ext} outside the domain are given quantities.
- The convention used in the Fig. 3 is $u_n = u = -\mathbf{u} \cdot \mathbf{n}$.
- The first wave λ_1 is a ghost wave, *i.e.* the pressure, the total enthalpy and the transported quantity are given at the inlet: $p_{b_{il}} = p_0 = p^{ext}$, $H_{b_{il}} = H_0 = H^{ext}$, $\psi_{b_{il}} = \psi_0 = \psi^{ext}$.
- The velocity at the inlet $u_{b_{il}} = u_0$ is positive so that the second, the third and the fourth waves, $\lambda_2(\mathbf{w}) = \lambda_3(\mathbf{w}) = u_0 \geq 0$ and $\lambda_4^-(\mathbf{w}) = u_0 + c_1 > u_0 = \lambda_2(\mathbf{w})$, are in the right part of the domain.

With these assumptions, static pressure and total enthalpy for the 0 state are known, which means that calculating u_0 leads to the static enthalpy, and thus to all the other thermodynamic variables using the real gas law. Calculating the 0 state means knowing the behavior of the fourth wave (the second wave is a contact discontinuity so that $p_1 = p_0$ and $u_1 = u_0$). For that matter, some tests on the first cell pressure are needed.

- First case: $p_0 > p_i^n$: the fourth wave is a 4-shock wave. Rankine-Hugoniot relations have to be used.
- Second case: $p_0 \leq p_i^n$: the fourth wave is a 4-expansion wave. Riemann invariants associated with this wave have to be used.

Once the calculation of u_0 is done, one must check whether the *scenario* is validated, *i.e.* $u_0 \geq 0$. If not, another *scenario* has to be considered. The details of the calculations and of the second and third *scenario* needed for the sake of completeness are given in the following sections. Note that for the transported quantity, the

calculations are straightforward since the solution of the Riemann problem for ψ is ψ^{ext} at the left of the contact discontinuity (second wave) and ψ_i^n at the right; thus, without any ambiguity we will not mention it in the following sections.

4.1.1 First case: 4-shock wave

Rankine-Hugoniot relations may be written:

$$\begin{cases} \rho_i^n (u_0 - u_i^n)^2 = (p_0 - p_i^n) (1 - \rho_i^n \tau(p_0, h_1)), \\ e_1 - e_i^n = -\frac{p_0 + p_i^n}{2} \left(\tau(p_0, h_1) - \frac{1}{\rho_i^n} \right). \end{cases} \quad (50)$$

The unknown is (u_0, h_1) . Using those relations and $h = e + p\tau$, one can use the following function to calculate h_1 :

$$G(h_1) = 2h_1 + \tau(p_0, h_1)[p_i^n - p_0] + \tau_i^n[p_i^n - p_0] - 2h_i^n = 0. \quad (51)$$

Providing that this equation admits a unique solution (see appendix 3 for a sketch of the proof), the calculation of the static enthalpy h_1 may be done using a secant method for example. Then, u_0 can be deduced easily using the first equation of (50) with $u_0 \geq u_i^n$ for a 4-shock wave.

4.1.2 Second case: 4-expansion wave

For the fourth wave, associated Riemann invariants may be written:

$$s_1 = s_i^n, \quad (52)$$

$$u_0 - \int_0^{\rho_1} \frac{c}{\rho} d\rho = u_i^n - \int_0^{\rho_i^n} \frac{c}{\rho} d\rho. \quad (53)$$

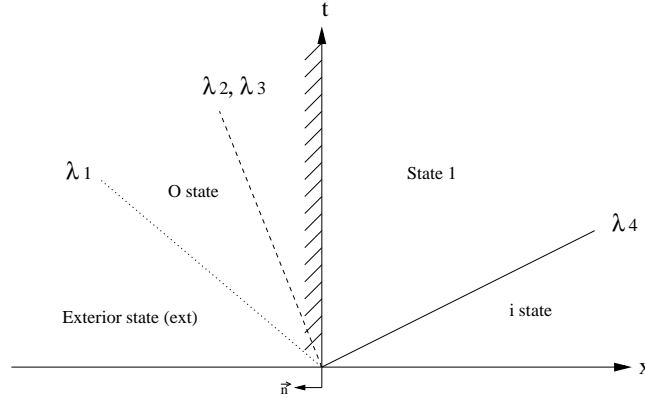
From (52), it is possible to write:

$$\begin{cases} \tau_1 = \tau(p_1, s_1) = \tau(p_0, s_i^n), \\ c_1^2 = c^2(p_1, s_1) = c^2(p_0, s_i^n). \end{cases}$$

Thus (53) gives the unknown $u_0 = u_i^n + \int_{\rho_i^n}^{\rho_1} \frac{c}{\rho} d\rho$. In practice, this integral may be evaluated thanks to a trapezoidal rule (which is second order accurate and sufficient for boundary conditions):

$$u_0 = u_i^n + \frac{1}{2} \left[\left(\frac{c}{\rho} \right)_i^n + \left(\frac{c}{\rho} \right)_1 \right] (\rho_1 - \rho_i^n). \quad (54)$$

Note that this formula is explicit contrary to what was obtained in the previous shock wave case.


 Figure 4: Riemann problem at the inlet, second *scenario*

4.1.3 Validation of the *scenario* and possible new *scenario*

From those two cases, the velocity u_0 can be deduced. If the velocity u_0 is positive, the *scenario* is validated. But if it is not the case, another *scenario* must be proposed.

The new *scenario* is depicted on the Fig. 4. If u_0 is negative, state 1 has to be imposed at the boundary face. As the user gave two conditions (static pressure and total enthalpy), and since only one 4-wave has to be crossed, the problem is over-constrained. Only one of the two information must be used. Since in this new *scenario*, the contact discontinuity is now at the left of the boundary face, we don't have anymore $H_{b_{il}} = H_0$, but we still have $p_{b_{il}} = p_0$. The natural choice is thus to keep the static pressure and ignore the total enthalpy. In this case, previous calculations are still valid and we can deduce $u_0 = u_1$ from p_0 (in section 4.1.1 and section 4.1.2, H_0 is only used at the end of the calculations to deduce the state 0 from p_0 and $u_0 = u_1 > 0$), but only if the fourth wave has a positive characteristic velocity which is either the velocity of the shock wave, $\sigma_4 > 0$, or the velocity at the left of the expansion 4-wave $u_1 + c_1 > 0$ (see Fig. 4), the velocity of the 4-shock wave being given by:

$$\sigma_4 = \frac{[\rho u]}{[\rho]} = \frac{\rho_i^n u_i^n - \rho_1 u_1}{\rho_i^n - \rho_1}. \quad (55)$$

Let's define the pressure ratio $y = p_i^n / p_0$. Two cases have to be considered:

1. $y < 1$:

The fourth wave is a 4-shock wave. Rankine relations must be used to get u_0 from $h_1 \rightarrow \rho_1 \rightarrow u_1 \rightarrow u_0$ as explained in section 4.1.1. Then, a test on the velocity u_0 is done.

• $u_0 \geq 0$:

The first *scenario* is valid, and state 0 is imposed at the cell interface using at the end of the calculations:

$$h_0 = H_0 - \frac{1}{2}u_0^2, \text{ and } \rho_0 = \frac{1}{\tau(p_0, h_0)}, \quad (56)$$

A simple binary search algorithm method on the interval $[p_0; p_i^n]$ is enough to get the solution $p^\#$. Indeed, we have:

$$\frac{d\mathcal{I}}{dp}(p) = \frac{\partial c}{\partial p}(p, s_i^n) + \frac{\tau(p, s_i^n)}{c(p, s_i^n)} > 0, \quad (59)$$

since $\frac{\partial c}{\partial p}|_s$ is a strictly positive function for the IAPWS real gas (for an ideal gas $\frac{\partial c}{\partial p}|_s = \frac{\gamma-1}{2\rho c} > 0$, with γ the classical adiabatic coefficient).

Moreover $\mathcal{I}(p_i^n) * \mathcal{I}(p_0) < 0$:

$$\mathcal{I}(p_i^n) = c_i^n + u_i^n > 0, \quad (60)$$

$$\mathcal{I}(p_0) = \mathcal{I}(p_1) = c_1 + \int_{\rho_i^n}^{\rho} \left(\frac{c}{\rho} \right) d\rho + u_i^n = c_1 + u_1 + \int_{\rho_i^n}^{\rho} \left(\frac{c}{\rho} \right) d\rho + u_i^n - u_1 = c_1 + u_1 < 0, \quad (61)$$

thanks to the hypothesis used for this third *scenario* (see Fig. 5) and the use of the Riemann invariants (57). Thus, this last result ensures the existence and the uniqueness of the zero of the function $\mathcal{I}(p)$ on the interval $[p_0; p_i^n]$.

In practice, one has to numerically evaluate the integral in (58) and we have used a trapezoidal rule in our code. However, it must be checked that the chosen numerical accuracy ε of the numerical method used to evaluate the integral ensures that $\varepsilon < |u_1 + c_1|$, otherwise one may encounter some difficulties to find the zero.

4.2 Supersonic outlet

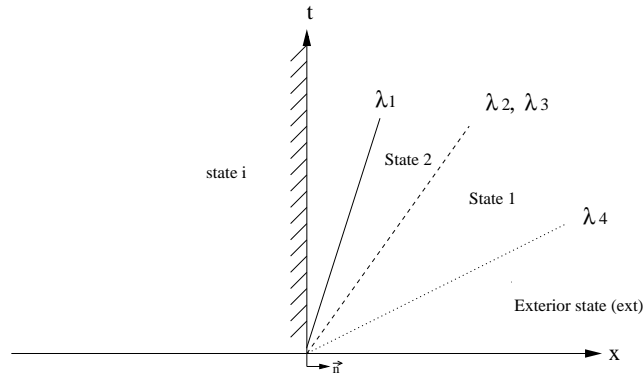


Figure 6: Riemann problem at the outlet, supersonic conditions

For a supersonic outlet, we consider the *scenario* depicted on Fig. 6. The *scenario* for this boundary condition is based on the following assumptions:

- No information is known outside of the domain.
- The convention used in the Fig. 6 is $u_n = u = \mathbf{u} \cdot \mathbf{n}$.
- The flow is considered to be supersonic at the outlet so that $u_i^n \geq c_i^n$. Thus, all the waves are outside the domain, $\lambda_1(\mathbf{w}) = u_i^n - c_i^n \geq 0$ and $\lambda_4(\mathbf{w}) \geq \lambda_2(\mathbf{w}) = \lambda_3(\mathbf{w}) \geq \lambda_1(\mathbf{w})$.

With these assumptions, the state at the boundary face is known and we have $\mathbf{Y}_{b_{il}}^* = (s_{b_{il}}, (u_n)_{b_{il}}, p_{b_{il}}, \psi_{b_{il}}) = (s_i^n, (u_n)_i^n, p_i^n, \psi_i^n)$. This *scenario* is validated as soon as $u_i^n \geq c_i^n$. However, as no information is known outside the domain, no other possible *scenario* can be considered. Indeed, as soon as the first wave enters the computational domain (*i.e.* $u_i^n < c_i^n$), one information is needed to fulfill a new *scenario*.

5 Results

This section is dedicated to the verification and the validation cases. First, classical verification tests based on one-dimensional Riemann problems will be considered (section 5.2). Then, some academic condensing supersonic nozzle tests will be introduced (section 5.3), in order to validate the condensation models (see section 1). In the framework of this paper, we have decided to compute one-dimensional nozzle flows. To do so, smooth section variations must be taken into account within the general formalism introduced in sections (1), (4) and (3). This is the object of the following section (5.1).

5.1 Equation system including smooth section variations

Experiments on steam condensation are mostly based on supersonic nozzles. In order to validate the models introduced before (see section 1), a one-dimensional code for smooth variable cross sections has been developed, based on the ideas presented before. The code solves the following equations (see [Anderson 95] or [Toro 09] for more details):

$$\begin{cases} \frac{\partial A}{\partial t} = 0, \\ \frac{\partial(\rho A)}{\partial t} + \frac{\partial \rho u A}{\partial x} = 0, \\ \frac{\partial(\rho u A)}{\partial t} + \frac{\partial(\rho u^2 + p)A}{\partial x} = +p \frac{\partial A}{\partial x}, \\ \frac{\partial(\rho E A)}{\partial t} + \frac{\partial(\rho E + p)u A}{\partial x} = 0, \\ \frac{\partial(\rho \psi A)}{\partial t} + \frac{\partial \rho u \psi A}{\partial x} = \mathbf{S}(\mathbf{w}), \end{cases} \quad (62)$$

where $A(x)$ is the smooth variable cross section, u the velocity, $E = u^2/2 + e(p, s)$ the total energy, $e(p, s)$ the internal energy defined by the real gas law (see section 2). The number q of transported variables $\boldsymbol{\psi} = \{\psi_k\}_{k=1..q}$ and the source term $\mathbf{S}(\mathbf{w})$ depend on the choice of the condensation model. We use either the simple non-equilibrium model with two additional transported variables (see equations (4)) or the QMOM model with twelve moments as additional transported variables (see equations (16)). We formally write the system (62):

$$\begin{cases} \frac{\partial A}{\partial t} = 0, \\ \frac{\partial(A\mathbf{w})}{\partial t} + \frac{\partial(A\mathbf{F}(\mathbf{w}))}{\partial x} = \mathbf{S}_A(\mathbf{w}), \end{cases}$$

with $\mathbf{w} = (\rho, \rho u, \rho E, \rho \boldsymbol{\psi})$, $\mathbf{F}(\mathbf{w})$ the associated flux function and the source term $\mathbf{S}_A(\mathbf{w}) = {}^t(0, p \frac{\partial A}{\partial x}, 0, \mathbf{S}(\mathbf{w}))$. We consider here a uniform one dimensional mesh in space and time, with constant space step Δx and time step Δt . The coordinate of

the center of each cell is x_i and of each face $x_{i+\frac{1}{2}}$. If we integrate the former system over each cell $\Omega_i = [x_{i-\frac{1}{2}}, x_{i+\frac{1}{2}}]$, we obtain the following explicit numerical scheme:

$$\begin{cases} A_i^{n+1} = A_i^n = A_i, \\ \mathbf{w}_i^{n+1} - \mathbf{w}_i^n + \lambda_i \left((\mathbf{AF}^{num}(\mathbf{w}_i^n, \mathbf{w}_{i+1}^n))_{i+\frac{1}{2}} - (\mathbf{AF}^{num}(\mathbf{w}_{i-1}^n, \mathbf{w}_i^n))_{i-\frac{1}{2}} \right) = \lambda_i \mathbf{S}_A^{num}(\mathbf{w}_i^n), \end{cases} \quad (63)$$

with $\mathbf{S}_A^{num}(\mathbf{w}_i^n) = {}^t(0, p_i^n \frac{A_{i+1} - A_{i-1}}{2}, 0, \mathbf{S}(\mathbf{w}_i^n) \Delta x)$ and λ_i taking, in this case, the particular form :

$$\lambda_i = \frac{\Delta t}{A_i \Delta x}.$$

Due to the section variations, the dimension of λ_i is not the one of a velocity. We now have to detail the numerical flux used in this scheme. For that matter, we first consider the Riemann problem located at the face $i + \frac{1}{2}$ and associated with the system (62) with the following initial condition:

$$\begin{cases} (A_l; \mathbf{w}_l) = \left(A_{i+\frac{1}{2}}^-; {}^t(\rho_i^n, (\rho u)_i^n, (\rho E)_i^n, (\rho \psi)_i^n) \right), \\ (A_r; \mathbf{w}_r) = \left(A_{i+\frac{1}{2}}^+; {}^t(\rho_{i+1}^n, (\rho u)_{i+1}^n, (\rho E)_{i+1}^n, (\rho \psi)_{i+1}^n) \right). \end{cases}$$

As the variable cross section $A(x)$ is smooth enough (typically $A(x)$ is a function $\mathcal{C}^2(\mathbb{R})$), we make the assumption that $A_{i+\frac{1}{2}}^- = A_{i+\frac{1}{2}}^+ = A_{i+\frac{1}{2}}$ so that A is a constant for the Riemann problem under consideration. \bar{A} is no longer an unknown and this Riemann problem thus reduces to the classical Riemann problem of the Euler system (with q transported variables) for the initial condition $(\mathbf{w}_l, \mathbf{w}_r)$. With this assumption, we can use the flux defined in the previous sections and write:

$$[\mathbf{AF}^{num}(\mathbf{w}_i^n, \mathbf{w}_{i+1}^n)]_{i+\frac{1}{2}} = A_{i+\frac{1}{2}} \mathbf{F}^{VF\text{Roe}}(\mathbf{w}_i^n, \mathbf{w}_{i+1}^n) = A_{i+\frac{1}{2}} \mathbf{F}(\mathbf{Y}_{i+\frac{1}{2}}^{*,n}),$$

using without any ambiguity the same notations as the previous sections. It remains to give the definition of the cross section at each face, for example $A_{i+\frac{1}{2}} = (A_i + A_{i+1})/2$ for an inner face, and at the boundary, the cross section of the corresponding cell next to it. This numerical scheme is classical for smooth cross sections. For a survey of numerical schemes adapted to smooth cross sections see [Faucher 00]. We insist here on the fact that the section is smooth enough so that there is no issue with discontinuities in the nozzle. For discontinuous cross sections and the related issues, the reader is referred to the references given in [Faucher 00]. In particular, a fine way to deal with discontinuous cross sections is to adopt the ideas developed by Greenberg-Leroux [Greenberg 96] based on the resolution of the Riemann problem of the complete system (62) where the non conservative product is written $p \frac{\partial A}{\partial x} = \frac{\partial(pA)}{\partial x} - A \frac{\partial p}{\partial x}$. A stationary wave associated with the variable $A(x)$ has to be considered, the non conservative product $A \frac{\partial p}{\partial x}$ being always well defined as for the stationary wave, where A is discontinuous, the formulation of the Riemann invariants associated with this wave is unique, and for the other waves A is continuous.

In the following, we present a verification one-dimensional test case (with a constant section) and three one dimensional validation test cases on steam condensation in nozzles in order to validate the scheme (63) associated with the boundary conditions described in section 4.

5.2 Verification tests for the VFRoe scheme with real gas law

In order to check the accuracy of the VFRoe scheme using the IAPWS-IF97 real gas equation of state, classical one dimensional test cases based on Riemann problems have been considered using both tabulated and polynomial versions of the equation of state. The table used hereafter has been generated using a 1.10^{-3} bar wide step for the pressure and a 0.25 K wide step for the temperature. In order to reach convergence, different one dimensional mesh sizes have been used (128, 256, 512, 1024, 2048, 4096, 8192 and 16384 cells for the contact discontinuity and the double shock cases, and up to 131072 cells for the double symmetric expansion wave and the shock tube cases). For meshes with more than 16384 cells, only the tabulated version of the code has been used. The space step of each mesh is uniform and we note N_c the number of cells for each mesh. Initial discontinuities are enforced at the middle of a 400 meters long domain (we note Lx the length of the computational domain), and the integration time lasts 0.20 seconds. Each simulation has been run using $CFL = 0.5$ and first-order schemes in time and space. With these parameters, the different waves of the solution never cross the left and right boundaries during the computation. Initial conditions for each case are given below :

Contact discontinuity (CD):

$$\begin{cases} \rho = 0.6 \text{ for } x < Lx/2 \text{ and } \rho = 0.45 \text{ for } x > Lx/2, \\ u = 100, \\ P = 10^5. \end{cases}$$

Double symmetric expansion wave (DSE):

$$\begin{cases} \rho = 0.6, \\ u = -100 \text{ for } x < Lx/2 \text{ and } u = 100 \text{ for } x > Lx/2, \\ P = 10^5. \end{cases}$$

SOD type shock-tube with a subsonic expansion wave (ST):

$$\begin{cases} \rho = 0.6 \text{ for } x < Lx/2 \text{ and } \rho = 0.3 \text{ for } x > Lx/2, \\ u = 0, \\ P = 1 * 10^5 \text{ for } x < Lx/2 \text{ and } P = 5 * 10^4 \text{ for } x > Lx/2. \end{cases}$$

Double symmetric shock wave (DSS):

$$\begin{cases} \rho = 0.45, \\ u = 100 \text{ for } x < Lx/2 \text{ and } u = -100 \text{ for } x > Lx/2, \\ P = 10^5. \end{cases}$$

Analytical solution has been computed using an exact real-gas Riemann solver described in appendix 5 for the IAPWS real gas law, with both polynomial and tabulated equations of state, in order to compare results using strictly identical EOS.

For each uniform mesh, we calculate the L1 error at time t^n for the variable ϕ thanks to this formula:

$$\|\phi_{exact} - \phi_{computed}\|_{L1} = \frac{\sum_{i=1}^{N_c} (|\phi_{exact}(x_i, t^n) - \phi_i^n|)}{\sum_{i=1}^{N_c} (|\phi_{exact}(x_i, t^n)|)}, \quad (64)$$

where x_i is the gravity center of the cell Ω_i . The obtained orders of convergence for both the tabulated and the polynomial EOS have been found to be identical, at least for meshes up to 16384 cells. Results corresponding to the finest meshes (tabulated EOS) are given in table 2.

	CD	DSE	ST	DSS
ρ	0.500	0.845	0.636	0.985
u	0.490	0.849	0.870	0.997
P	0.483	0.849	0.883	0.986

Table 2: Orders of convergence for tabulated EOS

The order of convergence are computed using the two finest meshes. For all the other meshes, it has been checked that, for meshes until 16384 cells, the L1 error is identical between both EOS (for the finer meshes on the double symmetric expansion wave and the shock tube cases, only the tabulated EOS has been used).

The asymptotic rate of convergence is the one that is expected for first-order schemes [Gallouët 02], *i.e.* 1 for the double symmetric shock wave and the double symmetric expansion wave, 0.5 for the contact discontinuity. In practice, for the size of the meshes used here, the asymptotic rate of convergence is achieved for the shock wave and the contact discontinuity, but for expansion wave, we classically obtain a rate close to 0.8.

The numerical verification cases are satisfactory, showing the ability of the VFRoe scheme to handle the complex thermodynamics and ensure the good numerical behavior of the code with the use of a tabulated equation of state. Results for the SOD-type shock-tube are plotted on Fig. 7 and Fig. 8. See appendix 4 for a contact discontinuity, a double symmetric shock wave and a double symmetric expansion wave.

The next three sections are dedicated to the application of the non-equilibrium condensation models to test cases in supersonic nozzles. For both steady and unsteady calculations, mesh convergence studies have been performed, leading to uniform meshes of 4000 cells for both steady and unsteady calculations, with a CFL number fixed to 0.5.

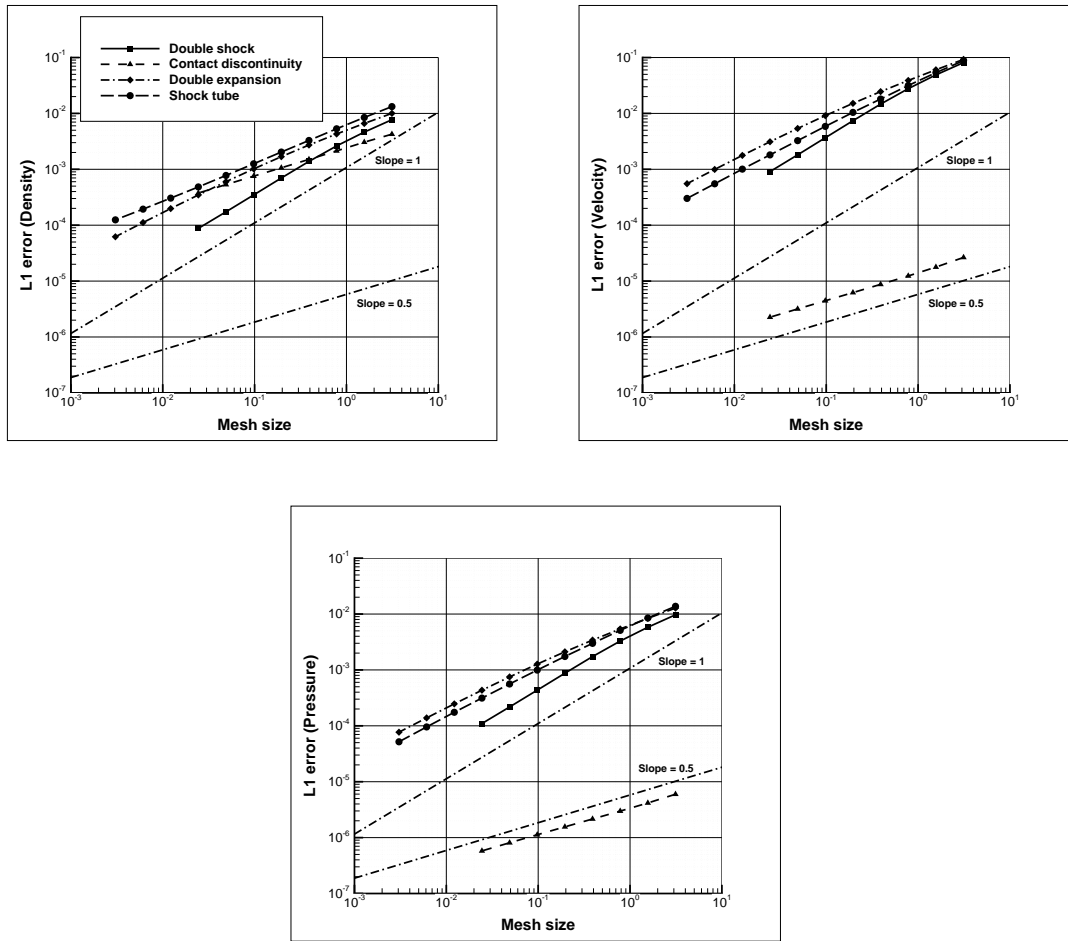
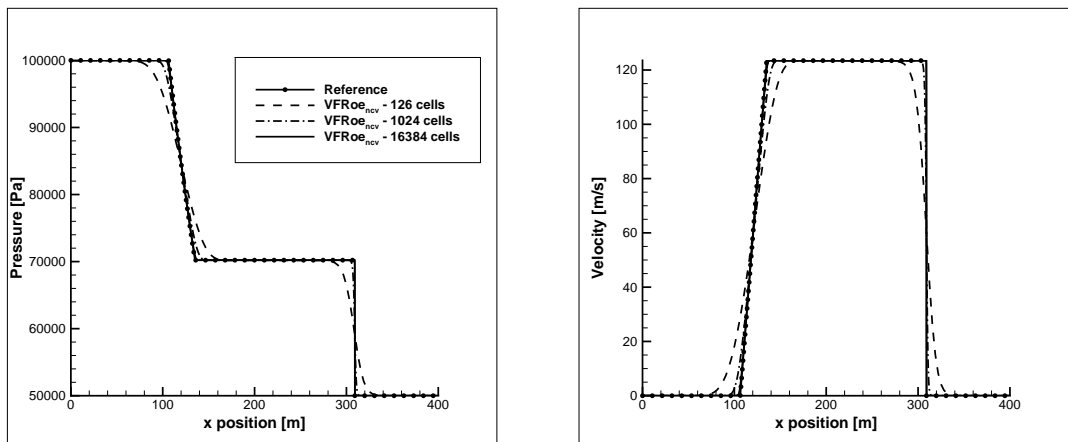


Figure 7: L1 errors for the VFRoe test cases using tabulated EOS (density, velocity and pressure)



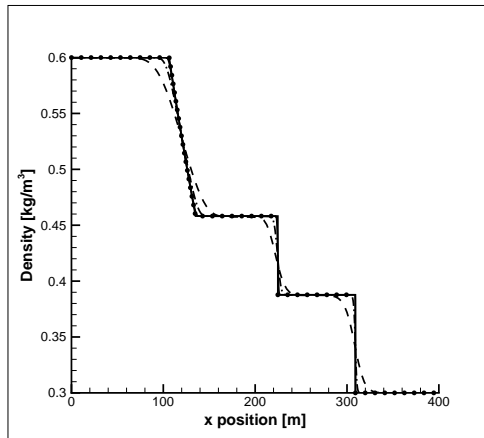


Figure 8: Comparison of pressure, velocity, and density profiles to the analytical solution in a shock-tube using VFRoe and the tabulated IAPWS EOS

5.3 Supersonic condensing nozzle tests

5.3.1 Moore's nozzle

During the last decades, some academical test cases dealing with steam condensation in nozzles have been published in the literature. One of the most well-known test cases is the Moore nozzle [Moore 73]. For this test case, a supersonic converging/diverging nozzle is used with a free supersonic outlet. The static pressure in the nozzle and droplet's mean radius close to the outlet have been measured. The flow in this nozzle is supposed to be steady, with a sub-critical heat release due to condensation, which means that the flow remains supersonic in spite of the appearance of condensation. Results are presented for nozzle B: the geometry used here is extracted from reference [Young 76]. First, the QMOM and the two-equation model predictions are confronted to the experimental data (Fig. 10). Twelve moments and six radii have been used with the QMOM. A mesh study has been performed using the QMOM method in order to determine the best agreement between computational time and accuracy of the results in an industrial framework (Fig. 9). As stated before, uniform meshes of 4000 cells have been used, which seems to be a good approximation of the solution, regarding the computational time (the variation of mean radius is below one percent between the 4000 cell and the 8000 cell meshes).

For both models, the expansion in the nozzle is very well predicted (Fig. 10): calculations are very close to the static pressure measurements in the condensation zone. Some small differences appear between the two-equation and the QMOM method. This is due to the computation of the growth of the liquid phase, that is based on one averaged radius for the two-equation model, and on the six computed radii for the QMOM. The position of the Wilson point *i.e.* the point where nucleation occurs, (on Fig. 10, this point is associated with the change of slope of the pressure curve) is not impacted by the model, as the nucleation rate is the same in both methods. In terms of mean radii (Fig. 10), the predictions of both models are also

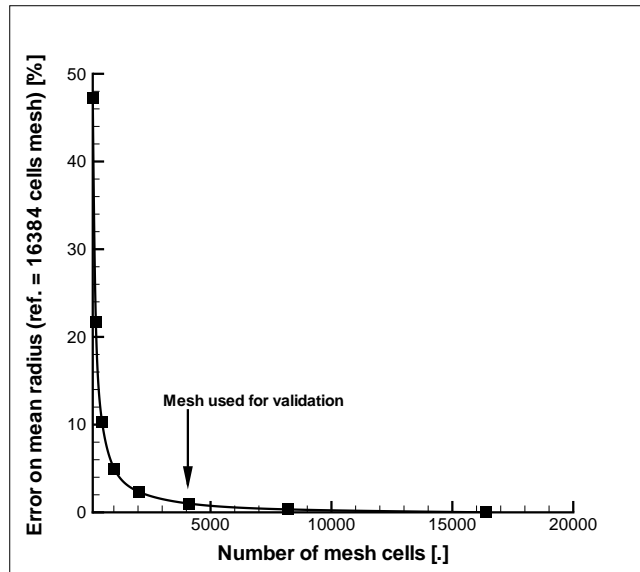


Figure 9: Convergence study for the sub-critical heat addition test case

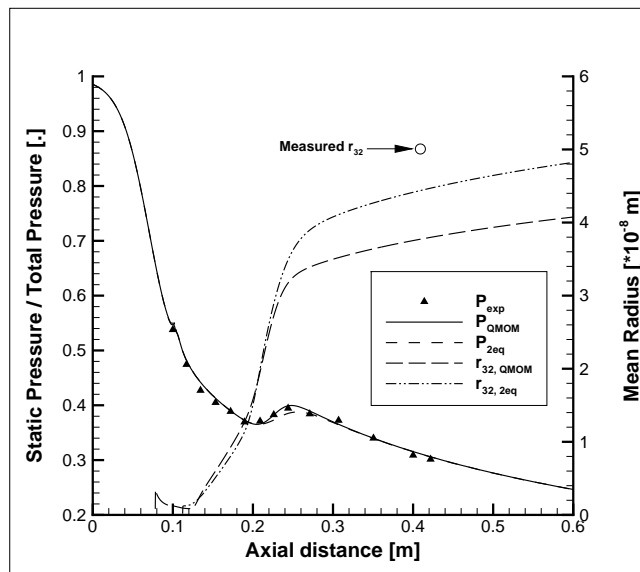


Figure 10: Comparison of the pressure expansion and mean droplet radius with experimental data, QMOM and two-equation model

good. The experimental measurements give an average radius size of $5 \times 10^{-2} \mu\text{m}$. The predicted radius is $4 \times 10^{-2} \mu\text{m}$ and $4.6 \times 10^{-2} \mu\text{m}$ with the two-equation model and the QMOM method respectively. Those results are rather good taking the measurement uncertainties into account.

For the QMOM method, the droplet spectrum that has been represented using

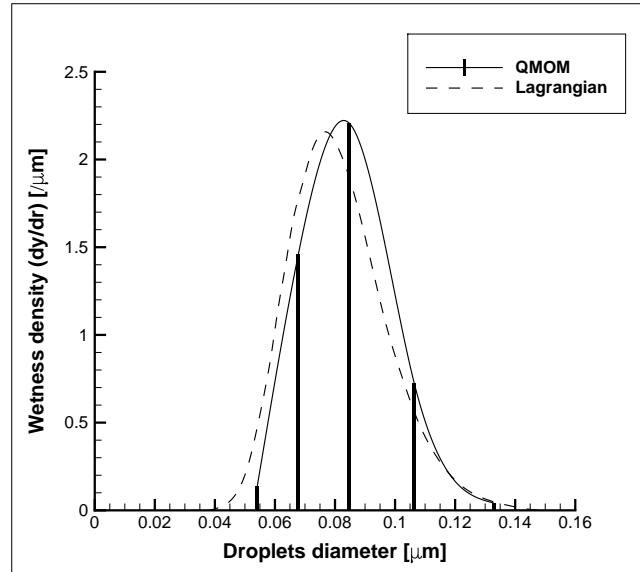


Figure 11: Comparison of the droplet spectrum computed with QMOM using 12 moments and a Lagrangian calculation by Young

a spline interpolation technique between computed radii, is compared with a spectrum [White 03] computed with the help of a Lagrangian method (Fig. 11). The comparison between both spectra highlights the ability of the QMOM method to compute polydispersion accurately, spectra having very similar shapes and values (the aim here is to highlight the ability of the QMOM to produce physical spectra and not to compare an Eulerian method to a Lagrangian one, that is much more suited for those typical applications, but not necessarily for industrial applications).

5.3.2 Barschdorff's nozzle

Barschdorff's nozzle is also a well known test case, as experiments have been run for sub-, critical, and sup-critical heat release due to condensation [Barschdorff 70]. Here, only the second case for a critical heat release is presented (see [Blondel 12] for the sup-critical heat release case): the flow is supersonic at the throat, and an aerodynamic shock appears in the diverging part, the heat release due to condensation being critical. This aerodynamic shock is stable and located close to the throat.

Results are presented for the QMOM model. In this case, twelve moments have been used, for six computed radii. The total inlet temperature has been modified (lowered by 1 K) so that calculations fit the experimental data much better. This is still coherent with measurements, as the uncertainty in the inlet temperature is 1 Kelvin. Using this correction at the inlet, the shock appearing in the diverging part of the nozzle is caught almost perfectly (Fig. 12). Spectra have been computed at different locations of the diverging part (Fig. 12 for positions, Fig. 13 for spectra). There are no measurements of the radii available for this test case, so that results are only qualitative. However, even with a strong discontinuity, spectra can be

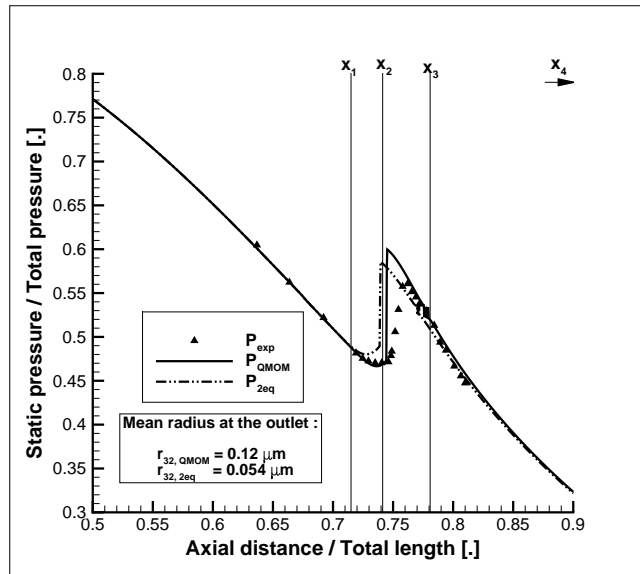


Figure 12: Pressure expansion in the Barschdorff's nozzle

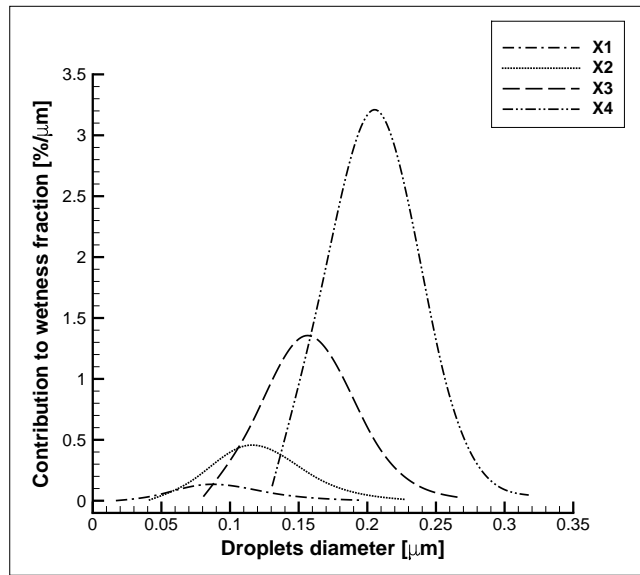


Figure 13: Droplet's spectra in the Barschdorff's nozzle

computed without any numerical difficulty, and show a typical behavior: they are shifted to the right (larger droplets) when moving downstream of the condensation shock, due to the droplet growth, and the amplitude of the spectrum increases, as bigger droplets lead to an increasing liquid mass fraction.

5.3.3 EDF nozzle tests

Some experiments have been run at EDF R&D, using three homothetic nozzles [Dorey 10] with expansion rates of 4000, 8000, and 16000 s^{-1} , for nozzles 1, 2 and 3, respectively. In these experiments, instability frequencies have been measured using a high speed camera. Those experiments are interesting to study the influence of the expansion rate on the droplet size distribution (Fig. 14 and 15). The droplet

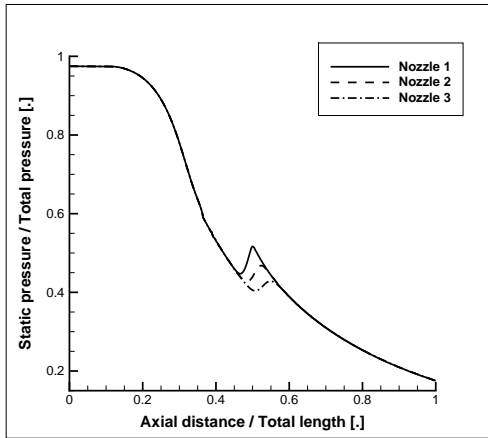


Figure 14: Pressure expansion computed in the 3 homothetic EDF nozzles

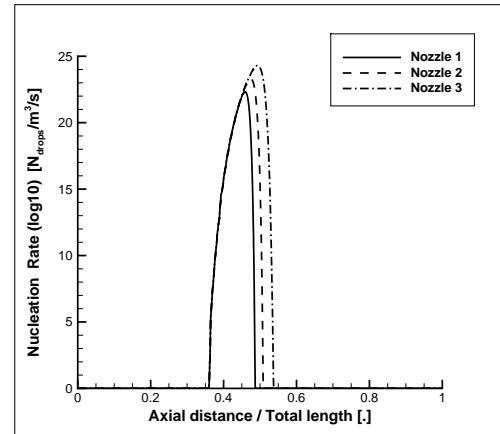


Figure 15: Nucleation rate computed in the 3 homothetic EDF nozzles

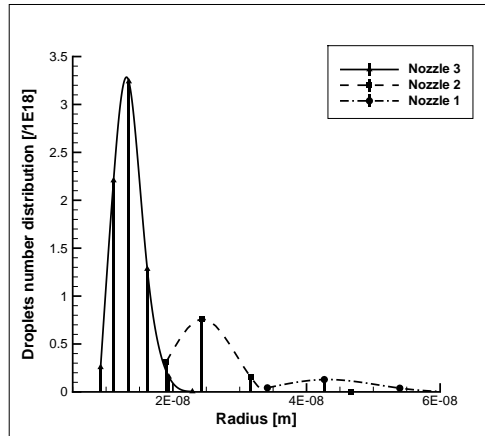


Figure 16: Comparison of the droplet spectra computed at the outlet of the EDF nozzles

spectra (Fig. 16) show a direct correlation between expansion rates and droplet sizes. For the highest expansion rate (nozzle 3), the subcooling at the Wilson point is the wider, involving a very high nucleation rate. Thus, a large number of tiny droplets will be created. For a smaller expansion rate, the subcooling is smaller, as

the expansion goes more slowly. Then, the nucleation rate is smaller, involving a smaller number of bigger droplets to be created in the flow. The lowest the expansion rate is, the flatter and the broader the droplet sizes distributions are (Fig. 16).

In the second calculation case for EDF's nozzles an aerodynamic shock appears in the diverging part of the nozzle, very close to the throat. As the heat release is sup-critical, the flow cannot absorb the total enthalpy rise, and the shock wave moves upstream, where the heat release is less important. With a shock wave crossing the throat, the nozzle is no longer adapted, and mass-flow rate fluctuations are noticed at the outlet of the nozzle. Then, the moving shock disappears in the converging part where the flow is supercooled, and a new cycle appears (Fig. 18). Validation consists in calculating the frequency of this phenomenon, which has been measured with a high speed camera during the experimentation. Once again, a mesh study has been performed for this computational case, in order to highlight the influence of the mesh on the moving shock wave frequency (Fig. 17) using the QMOM method. This

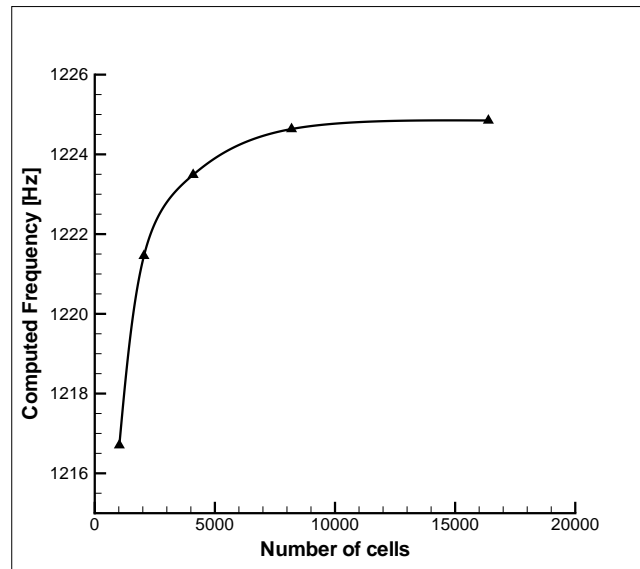


Figure 17: Convergence study for the sup-critical heat addition test case

study shows that frequency variations regarding the mesh are almost negligible for at least 4000 mesh cells (between the 4000 and the 16000 mesh cells calculations, the frequency variation is about $1.36Hz$, which represents a difference of 0.11%). Thus, the size of the mesh used here is the same than for the steady calculations (4000 cells). For the sup-critical heat release, frequencies have been measured experimentally, but there are no measurements of the droplet sizes, neither of the static pressure. Using both the QMOM and the two-equations model, the frequency of the moving shock is caught pretty well compared with experimental data (table 3).

Some small discrepancies appear on the frequencies between both models, due to the computation of the growth law, based on a single average radius size for the two-equation model, and on several representative radii for the QMOM method. As there were no measurements of the droplet spectrum, the distributions presented in

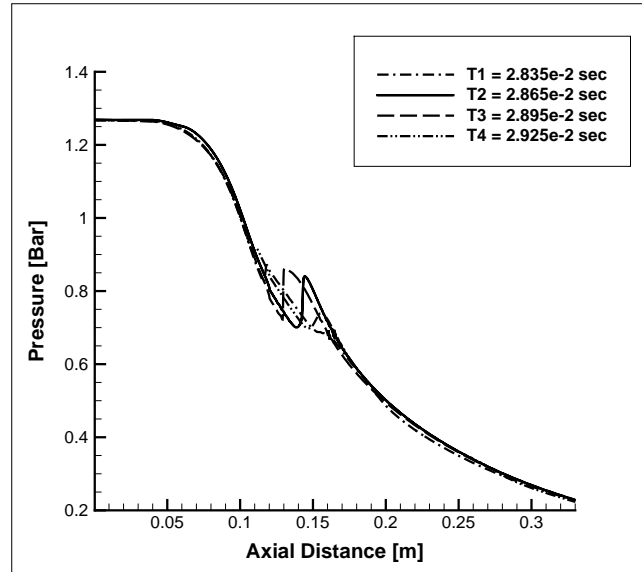


Figure 18: Pressure expansion during an instability cycle

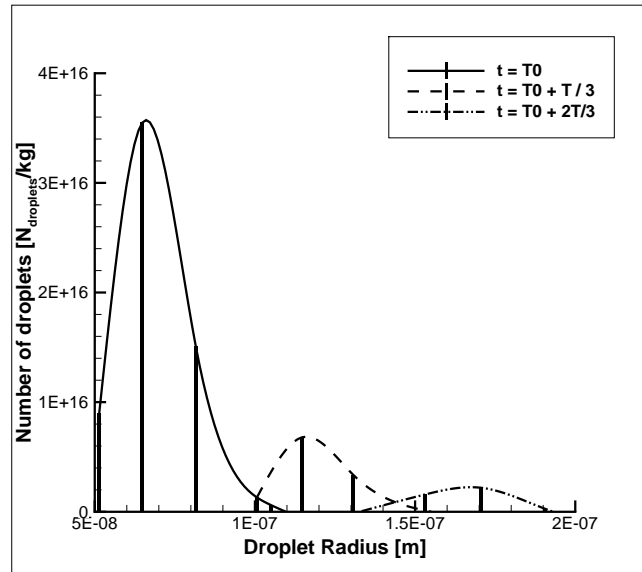


Figure 19: Droplet spectrum evolution at the outlet during an instability cycle

	Measurement:	2_{eq} model:	QMOM
Frequency:	1170 Hz	1161 Hz	1220 Hz
Error:	0	< 1%	4.3%

Table 3: Measured and computed frequencies of the instability in the EDF's nozzle

Fig. 19 cannot be validated. The results show that the droplet spectrum suffers from very strong variations in terms of droplet numbers and sizes. The radii are included in a range from 50 to 200 nano-meters, while droplets number are varying with more than one order of magnitude. Those highly unsteady flows have been handled without any difficulty using the VFRoe scheme.

Conclusion

This paper was devoted to the physical and numerical modelling of wet steam flows with non-equilibrium condensation in power plant steam turbines. In such turbines, the steam behavior is far from the one of an ideal gas and real gas thermodynamic laws have to be considered. In this paper we have chosen the IAPWS-IF97 formulation which deals with both equilibrium and non-equilibrium wet steam flows. The nucleation process has been taken into account thanks to two models: a simple two-equation model and a more advanced one, namely the Quadrature Method of Moments (QMOM); we recall that the QMOM model is the only one that takes polydispersion into account. In order to handle this model, a VFRoe scheme has been used since it is well suited for real gas thermodynamics. However, a different strategy has been adopted to define the flux at the boundaries: a Godunov flux has been used with the resolution of exact half Riemann problems depending on the number of known information at a given boundary of the domain. Two kinds of boundary conditions have been detailed in the paper: a constant pressure and constant enthalpy subsonic inlet condition and a supersonic outlet condition, since only these two conditions are needed to solve the nozzle test cases presented here. For the sake of completeness two other boundary conditions have been detailed in the appendix: a constant pressure subsonic outlet condition and an adiabatic wall condition. The constant pressure subsonic outlet condition can be combined with the supersonic outlet condition to give a general outlet condition. We have built different kinds of *scenarii* in order to uniquely define all these boundary conditions for general real gas laws. Finally, we have shown on numerical shock-tube verification test cases that the real gas VFRoe scheme retrieves the classical orders of convergence for contact discontinuities, double symmetric shock waves and double symmetric expansion waves. Moreover, thanks to three different supersonic nozzle flows, we have assessed the accuracy of the QMOM model to properly capture condensation shock, droplet spectra and even the frequency of an unsteady phenomenon such as the oscillation of a shock wave in presence of condensation. These results sound very promising for the implementation of this model in a tridimensional code and its application to the last stages of power plant steam turbines.

Acknowledgements

The first author received a financial support through an EDF-CIFRE contract 777/2011. All computational facilities were provided by EDF.

Bibliography

- [Anderson 95] Anderson J.D., (1995), "Computational Fluid Dynamics : The basics with applications". McGraw-Hill, Inc.
- [Bakhtar 05] Bakhtar F., Young J.B., White A.J., Simpson D.A., (2005), "Classical nucleation theory and its application to condensing steam flow calculations". Proc. of the IMechE., Vol. 219 pp. 1315-1333.
- [Barschdorff 70] Barschdorff D., (1970), "Droplet formation influence of shock waves and instationary flow patterns by condensation phenomena at supersonic speeds". 3rd Conf. on Rain Erosion, R.A.E. Farnborough, pp. 691-705.
- [Baumann 21] Baumann K., (1921), "Some recent developments in large steam turbine practice". Journal of Inst. Electr. Eng., Vol. 59, pp. 565-623.
- [Blondel 12] Blondel F., Fendler Y., Stanciu M., Dorey J.M., Lance M., Leboeuf F., Leonard O., (2012), "Mixed 1D-2D-3D approaches for wet steam modelling in steam turbines". Baumann centenary Conference, Cambridge, BCC-2012-06, <http://baumann.eng.cam.ac.uk/details/Prog>.
- [Buffard 00] Buffard T., Gallouët T., Hérard J. M., (2000), "A sequel to a rough Godunov scheme: application to real gases". Comp. and Fluids, Vol. 29 pp. 813-847.
- [Chandler 12] Chandler K., White A., Young J., (2012), "Comparison of unsteady non-equilibrium wet-steam calculations with model turbine data". Baumann centenary Conference, Cambridge, BCC-2012-10, <http://baumann.eng.cam.ac.uk/details/Prog>.
- [Coquel 98] Coquel F., Perthame B., (1998), "Relaxation of energy and approximate Riemann solvers for general pressure laws in fluid dynamics equations". SIAM J. Numer. Anal., Vol. 35(6), pp. 2223-2249. In memory of Ami Harten.
- [Coquel 12] Coquel F., Godlewski E., Seguin N., (2012), "Relaxation of fluid systems". Mathematical Models and Methods in Applied Sciences.
- [Dorey 10] Dorey J.M., Stanciu M., Ren K., (2010), "Experiments on steam condensation in a 3-scale nozzle vein using light extinction and a high speed camera". 7th Int. Conf. on Multiphase Flows, <http://ufdc.ufl.edu/UF00102023/00326/11j>.
- [Dubois 87] Dubois F. (1987), "Boundary conditions and the Oscher scheme for the Euler equations of the gas dynamics". CMAP Report n°170, Centre Mathématiques de l'école Polytechnique, Palaiseau, France.
- [Dykas 12] Dykas S., Wróblewski W., (2012), "Application of an in-house CFD code for steam flow modelling in a Baumann stage", Baumann centenary Conference, Cambridge, BCC-2012-02, <http://baumann.eng.cam.ac.uk/details/Prog>.
- [Faucher 00] Faucher E., Hérard J. M., Barret M., Toulemonde C. (2000), "Computation of flashing flows in variable cross section ducts". Int. J. of Comp. Fluid Dynamics, Vol. 13(4) pp. 365-391.
- [Gallouët 96] Gallouët T., Masella J. M., (1996), "Un schéma de Godunov approché". Comptes Rendus de l'Académie des Sciences, Paris, série I 323 pp. 77-84.
- [Gallouët 02] Gallouët T., Hérard J. M., Seguin N. (2002), "Some recent finite volume schemes to compute Euler equations using real gas EOS". Int. J. for Numerical Methods in Fluids, Vol. 39(12) pp. 1073-1138.
- [Gallouët 03] Gallouët T., Hérard J. M., Seguin N., (2003), " On the use of some

- symmetrizing variables to deal with vacuum". CALCOLO, Vol. 40 pp. 163-194.
- [Gerber 04] Gerber A.G., Kermani M.J., (2004), "A pressure based Eulerian-Eulerian multi-phase model for non-equilibrium condensation in transonic steam flows". Int. Journal of Heat and Mass Transfer, Vol. 47 pp 2217-2231.
- [Gerber 07] Gerber A. G., Mousavi A., (2007), "Application of the Quadrature-Method-of-Moments to the polydispersed droplet spectrum in transonic steam flows with primary and secondary nucleation". J. Appl. Math. Modelling, Vol. 31, pp. 1518-1533.
- [Glaister 88] Glaister P., (1988), "An approximate linearised Riemann solver for the the Euler equations for real gases". Journal of Computational Physics, Vol. 74, pp. 382-408.
- [Godlewski 96] Godlewski E., Raviart P.A. (1996), "Numerical Approximation of hyperbolic systems of conservation laws". Applied Mathematical Sciences 118, Springer Verlag.
- [Godunov 59] Godunov S.K., (1959), "A difference method for numerical calculation of discontinuous equations of hydrodynamics". Math Sbornik (in Russian), Vol. 47, pp. 217-306.
- [Greenberg 96] Greenberg J. M., Leroux A.Y., (1996)."A well balanced scheme for the numerical processing of source term in hyperbolic equations". SIAM J. Num. Anal., Vol. 33(1) pp 1-16.
- [Gyarmathy 62] Gyarmathy G. (1962). "Grundlagen einer Theorie der Nassdampf-turbine". PhD Thesis, Zürich, Juris-Verlag.
- [Halama 10] Halama J., Benkhaldoun F., Fort J., (2010), "Numerical Modelling of two-phase transonic flow". Mathematics and Computers in Simulation, Vol. 80, pp. 1624-1635.
- [Helluy 10] Helluy P., Hérard J.M., Mathis H., Müller S. , (2010), "A simple parameter-free entropy correction for approximate Riemann solver". C.R. Mécanique, Vol. 338 pp. 493-498.
- [IAPWS 07] (2007), "Revised release on the IAPWS industrial formulation 1997 for the thermodynamic properties of water and steam". <http://www.iapws.org>.
- [IAPWS 08] (2008), "Release on the IAPWS formulation 2008 for the viscosity of ordinary water substance". <http://www.iapws.org>.
- [IAPWS 11] (2011), "Release on the IAPWS formulation 2011 for the thermal conductivity of ordinary water substance". <http://www.iapws.org>.
- [John 12] John V., Thein F., (2012), "On the efficiency and robustness of the core routine of the quadrature method of moments (QMOM)". Journal of Chemical Engineering Science, Vol. 75 pp. 327-333.
- [Kantrowitz 51] Kantrowitz A., (1951), "Nucleation in very rapid vapor expansions". Journal of Chemical Physics, Vol. 19 pp. 1097-1100.
- [Kim 89] Kim Y.P., Seinfeld J.H., (1989), "Simulation of multicomponent aerosol condensation by the moving sectional method". Journal of Colloid and Interface Science, Vol. 135 pp. 185-200.
- [Lamanna 00] Lamanna G., (2000), "On nucleation and droplet growth in condensing nozzle flows". PhD Thesis, Eindhoven University of Technology, ISBN 90-386-1649-X
- [Marchisio 03] Marchisio D.L., Pikturna J.T., Fox R.O., Vigil R.D., Barresi A.A.,

- (2003), "Quadrature Method of Moments for population-balance equations". AICHE Journal, Vol. 49, pp. 1266-1276.
- [Marchisio 03b] Marchisio D.L., Vigil R.D., Fox O., (2005), "Quadrature method of moments for aggregation-breakage processes". Journal of Colloid and Interface Science, Vol. 258, pp. 322-334.
- [Marchisio 05] Marchisio D.L., Fox R.O., (2005), "Solution of population balance equations using the direct quadrature method of moments". Aerosol Science, Vol. 36, pp. 43-73.
- [Masella 99] Masella J. M., Faille I., Gallouët T., (1999), "On an approximate Godunov scheme". International Journal of Computational Fluid Dynamics, Vol. 12 pp. 133-149.
- [McGraw 97] McGraw R., (1997), "Description of aerosol dynamics by the quadrature method of moments". Aerosol Sci. and Tech., Vol. 27 pp. 255-265.
- [Moore 73] Moore M.J., Walters P.T., Crane R.I., Davidson B.J., (1973), "Predicting the fog-drop size in wet-steam turbines". Inst. Mech. Engrs., C37/73 pp. 101-109.
- [Press 92] Press W.H., Teukolsky S.A., Vetterling W.T., Flannery B.P., (1992), "Numerical recipes in Fortran". Second Edition, Cambridge University Press
- [Roe 81] Roe P. L., (1981), "Approximate Riemann solvers, parameter vectors and difference scheme". Journal of Computational Physics, Vol. 43 pp. 357-372.
- [Smoller 83] Smoller J., (1983), "Shock waves and reaction-diffusion equations". Springer Verlag.
- [Stastny 08] Stastny M., Sejna M., (2008), "Condensation of Water Steam with and without NaCl Impurity in a Nozzle". XV Int. Cond. on the Properties of Water and Steam, Berlin, <http://www.15icpws.de/>.
- [Toro 09] Toro E.F., (2009), Riemann Solvers and Numerical Methods for Fluid Dynamics: a practical introduction, Third Edition, Springer Verlag.
- [White 00] White A. J., (2000), "Modelling droplet size distributions in polydispersed wet-steam flows". Int. J. Numer. of Heat and Mass Transfer, Vol. 43 pp. 1873-1884.
- [White 03] White A. J., (2003), "A comparison of modelling methods for polydispersed wet-steam flow". Int. J. Numer. Meth. Engng, Vol. 57 pp. 819-834.
- [Young 76] Young J.B., Bakhtar F., (1976), "A comparison between theoretical calculations and experimental measurements of droplet sizes in nucleation steam flows". Prace Instytutu Maszyn Przeplywowych, pp. 259-271.
- [Young 82] Young J.B., (1982), "The spontaneous condensation of steam in supersonic nozzles". PhysicoChemical Hydrodynamics, Vol. 3, pp 57-82.

Appendix 1: Constant pressure subsonic outlet condition and general outlet condition

The subsonic boundary condition with an imposed static pressure is derived in a very similar way than the subsonic inlet boundary condition. In the sequel, the notations are those of Fig. 20, so that we are looking for the state 2 at the boundary face.

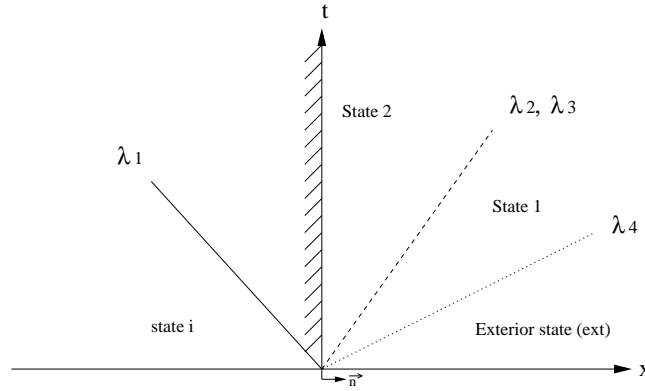


Figure 20: Riemann problem at the outlet, first *scenario*

The *scenario* for this boundary condition is based on the following assumptions:

- The pressure p^{ext} is a given quantity.
- The convention used in Fig. 20 is $u_n = u = \mathbf{u} \cdot \mathbf{n}$.
- The fourth wave λ_4 is a ghost wave, i.e. the pressure is given at the outlet ($p_{b_i} = p_2 = p_1 = p_{ext}$). Indeed, across the contact discontinuity we have $u_2 = u_1$ and $p_2 = p_1$.
- The flow is considered to be subsonic at the outlet so that $u_i^n < c_i^n$ and the first wave $\lambda_1(\mathbf{w}) = u_i^n - c_i^n < 0$ is on the left part of the domain. Moreover, the intermediate velocity u_2 is supposed to be positive, so that the second, the third and the fourth waves, $\lambda_2(\mathbf{w}) = \lambda_3(\mathbf{w}) = u_2 > 0$ and $\lambda_4^-(\mathbf{w}) = u_2 + c_1 > u_2 = \lambda_2(\mathbf{w})$, are on the right part of the domain.

With these assumptions, we need to evaluate the state 2 across the first wave, knowing $p_2 = p^{ext}$ and the left state in the last cell of the computational domain. Depending on the sign of $p_2 - p_i^n$, two cases have to be considered:

- First case: $p_2 > p_i^n$: the first wave is a 1-shock wave. Rankine-Hugoniot relations have to be used.
- Second case: $p_2 \leq p_i^n$: the first wave is a 1-expansion wave. Riemann invariants associated with this wave have to be used.

Once the calculation of u_2 is done, one must check that the *scenario* is validated, *i.e.* $u_2 \geq 0$. If not, another *scenario* has to be considered. The details of the calculations and of the possible new *scenario* needed for the sake of completeness are given below. The calculations for the first *scenario* are strictly the same as those for the inlet boundary condition. However, they are given here with the adapted notations for the constant pressure subsonic outlet condition.

First case: 1-shock wave

Rankine-Hugoniot relations might be written:

$$\begin{cases} \rho_i^n (u_2 - u_i^n)^2 = (p_2 - p_i^n) (1 - \rho_i^n \tau(p_2, h_2)), \\ e_2 - e_i^n = -\frac{p_2 + p_i^n}{2} \left(\frac{1}{\rho(p_2, h_2)} - \frac{1}{\rho_i^n} \right). \end{cases} \quad (65)$$

The unknown are (u_2, h_2) . Using those relations and $h = e + p\tau$, one can use the following function to calculate h_2 :

$$G(h_2) = 2h_2 + \tau(p_2, h_2)[p_i^n - p_2] + \tau_i^n [p_i^n - p_2] - 2h_i^n = 0 \quad (66)$$

Providing that this equation admits a unique solution (see appendix 3 for a sketch of the proof), the calculation of the static enthalpy h_2 may be done using a secant method for example. Then, u_2 can be deduced easily using the first equation of (65) with $u_2 \leq u_i^n$ for a 1-shock wave.

Second case: 1-expansion wave

For the first wave, associated Riemann invariants might be written using notations for the outlet:

$$s_2 = s_i^n, \quad (67)$$

$$u_2 + \int_0^{\rho_2} \frac{c}{\rho} d\rho = u_i^n + \int_0^{\rho_i^n} \frac{c}{\rho} d\rho. \quad (68)$$

From (67), it is possible to write:

$$\begin{cases} \tau_2 = \tau(p_2, s_2) = \tau(p_2, s_i^n), \\ c_2^2 = c^2(p_2, s_2) = c^2(p_2, s_i^n). \end{cases}$$

Thus (68) gives the unknown $u_2 = u_i^n + \int_{\rho_i^n}^{\rho_2} \frac{c}{\rho} d\rho$. In practice, this integral may be evaluated thanks to a trapezoidal rule (which is second order accurate and sufficient for boundary conditions):

$$u_2 = u_i^n - \frac{1}{2} \left[\left(\frac{c}{\rho} \right)_i^n + \left(\frac{c}{\rho} \right)_2 \right] (\rho_2 - \rho_i^n). \quad (69)$$

Note that this formula is explicit contrary to what was obtained in the previous shock wave case.

Validation of the scenario and possible new scenario

From the two previous cases, the velocity u_2 can be deduced. If the velocity is positive, the *scenario* is validated. If not, another *scenario* must be proposed. The new *scenario* is depicted on the Fig. 21. If the velocity u_2 is negative, state 1 has to be imposed at the boundary face. As the user gave only one condition (static

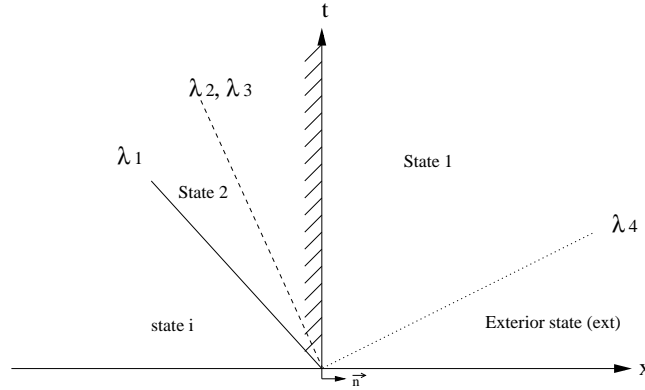


Figure 21: Riemann problem at the outlet, second *scenario*

pressure), and since two waves have to be crossed, the problem is under-constrained (the value of ρ_1 through the contact discontinuity is missing). The choice made here is to suppose that nothing happens across the contact discontinuity, so that we write:

$$\begin{cases} \rho_1 = \rho_2, \\ h_1 = h_2. \end{cases}$$

Thus, it is possible to calculate state 2 using previously introduced relations (66) or (69) and to impose state 1 (which is now equal to state 2) at the boundary face.

General outlet condition

Thanks to the previous constant pressure subsonic outlet and the supersonic outlet given in section 4.2, we can derive a general outlet condition which algorithm can be sum up the following way:

1. $\underline{u_i^n - c_i^n < 0}$: depending on the sign of $p_2 - p_i^n$, the first wave is either a 1-shock wave or a 1-expansion wave and u_2 can be deduced from (66) or (69). Two cases are to be considered:
 - (a) $\underline{u_2 \geq 0}$: the *scenario* depicted on Fig. 20 is validated and state 2 is imposed at the boundary face.
 - (b) $\underline{u_2 < 0}$: the *scenario* depicted on Fig. 21 may occur. As no information is known about ρ_1 , the choice we have made is to also impose state 2 at the boundary face.

2. $\underline{u_i^n - c_i^n \geq 0}$:

- (a) $\underline{p_2 \leq p_i^n}$: 1-expansion wave: the outlet is in fact supersonic and the *scenario* depicted on Fig. 6 is validated. The state at the boundary face is the interior state of the cell Ω_i at time t^n .
- (b) $\underline{p_2 > p_i^n}$: 1-shock wave: two cases are to be considered:
- $\sigma_1 \geq 0$: the outlet is in fact supersonic and the *scenario* depicted on Fig. 6 is validated. The state at the boundary face is the interior state of the cell Ω_i at time t^n .
 - $\sigma_1 < 0$: two cases have to be considered depending on the sign of u_2 :
 - $u_2 \geq 0$: the *scenario* depicted on Fig. 20 is validated and state 2 is imposed at the boundary face.
 - $u_2 < 0$: the *scenario* depicted on Fig. 21 may occur. As no information is known about ρ_1 , the choice we have made is to also impose state 2 at the boundary face.

Appendix 2: Adiabatic real gas wall condition

In this section, the notations are those of section 3 and 4. The original conservative variable is $\mathbf{w} = (\rho, \rho\mathbf{u}, \rho E, \rho\psi)$, but we remind that we consider the tangential velocities as a part of the vector ψ and that for the sake of simplicity, the vector ψ is considered as a scalar quantity ψ (the generalization of this section is however straightforward for q transported quantities). For an adiabatic wall, nothing is

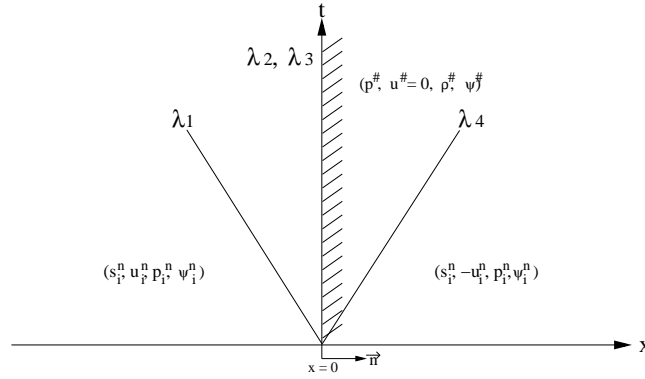


Figure 22: Riemann problem at the wall

known at the boundary except that no mass flux should cross the wall, *i.e.* $u_n = 0$, which is the natural physical condition for the velocity of Euler systems. The notations are those of Fig. 22. In order to determine the state at the wall, some assumptions have to be made:

- The convention used in the Fig. (22) is $u_n = u = \mathbf{u} \cdot \mathbf{n}$.
- Knowing the interior state at the left of the boundary face $(s_i^n, u_i^n, p_i^n, \psi_i^n)$, we suppose that the exterior state at the right is given by a mirror state $(s_i^n, -u_i^n, p_i^n, \psi_i^n)$. A straightforward calculation of the solution of the Riemann problem shows that, for such an initial condition, we have $u^\# = 0$ at the wall which thus explains the particular form chosen here for the right state.

With these assumptions, the normal flux at the wall takes the following particular form (see equation (31)):

$$\mathcal{F}(\mathbf{w}(\mathbf{x} = 0, t); \mathbf{n}) = \begin{pmatrix} 0 \\ p\mathbf{n} \\ 0 \\ \mathbf{0} \end{pmatrix}, \quad (70)$$

so that we only need to know the pressure $p^\#$ at the wall which is constant through the contact discontinuity for the two intermediate states of the Riemann problem at the wall. The structure of the solution of the Riemann problem at the wall depends on the velocity sign :

- Positive velocity ($u_i^n \geq 0$): double symmetric shock wave. Rankine-Hugoniot relations have to be used.
- Negative velocity ($u_i^n < 0$): double symmetric expansion wave. Riemann Invariants associated with the first (or the fourth) wave have to be used.

The existence and uniqueness of the Riemann problem with an initial condition given by the mirror states is proved if the following classical condition [Smoller 83] is achieved: $u_r - u_l < \int_0^{\rho_l} \frac{c(\rho, s_l)}{\rho} d\rho + \int_0^{\rho_r} \frac{c(\rho, s_r)}{\rho} d\rho$, otherwise $\rho^\# = 0$.

Once the pressure $p^\#$ is calculated (thanks to the appendix 5 for example), the flux is given by the classical Godunov flux.

In the code, we propose another choice to calculate the flux with the approximate Riemann solver VFRoe. For the linearized Riemann problem associated with the mirror state, we can deduce immediately the pressure $p^\#$ (see equations (39) and (40)):

For the double symmetric shock wave configuration :

$$p^\# = \min \left\{ p_{max}^{eos}; p_i^n \left[1 + \frac{\rho_i^n (c_i^n)^2}{p_i^n} M_i^n \right] \right\}, \quad (71)$$

and for the double symmetric expansion wave configuration :

$$p^\# = \max \left\{ p_{min}^{eos}; p_i^n \left[1 + \frac{\rho_i^n (c_i^n)^2}{p_i^n} M_i^n \right] \right\}, \quad (72)$$

where $M_i^n = u_i^n / c_i^n$ is the normal Mach number in the cell next to the wall and $[p_{min}^{eos}, p_{max}^{eos}]$ are the boundary values of the pressure given by the IAPWS equation of state. In the applications treated in this paper, the normal Mach number is very low close to the wall, so that using $p^\#$ from the linearized or the exact Riemann problem is almost equivalent.

The issue of the difference between the two approaches for all normal Mach numbers with an ideal polytropic gas has been considered in [Buffard 00]. In the appendix of this paper, it is shown that $p_{VFRoe}^\# / p_i^n$ is the limited development of $p_{Godunov}^\# / p_i^n$ up to first order with respect to the Mach number.

Appendix 3: Study of $G(h)$ function

In order to fulfill the requirements of the inlet and the outlet boundary conditions, it must be proved that the following function admits a unique zero in $]0, +\infty[$, so that it can be inverted using, for example, a Newton-Raphson method:

$$G(h) = 2h + \tau(p_0, h)[p_i^n - p_0] + \tau_i^n[p_i^n - p_0] - 2h_i^n = 0. \quad (73)$$

For that matter, we first make some usefull remarks. In the case of a shock wave (which is the only case of interest for the function $G(h)$), the pressure behind the shock is greater than the pressure upstream so that:

$$p_i^n - p_0 < 0. \quad (74)$$

Moreover, we have checked that for the IAPWS equation of state, the following assertions can be made, as long as the polynomial relations are used inside their definition domain (see section 2):

$$\left\{ \begin{array}{l} \left(\frac{\partial \tau}{\partial h} \right)_p > 0, \\ \left(\frac{\partial \tau}{\partial p} \right)_h < 0, \\ \left(\frac{\partial \tau^2}{\partial^2 h} \right)_h < 0. \end{array} \right. \quad (75)$$

Thanks to the relations (74) and (75), we can now study the variations of the function $G(h)$. The first derivative of $G(h)$ can be written (noting that $\tau_i^n[p_i^n - p_0] - 2h_i^n$ is a constant) :

$$G'(h) = 2 + \frac{\partial \tau}{\partial h}(p_0, h)(p_i^n - p_0), \quad (76)$$

and the second derivative of $G(h)$ is then:

$$G''(h) = \frac{\partial \tau^2}{\partial^2 h}(p_0, h)(p_i^n - p_0). \quad (77)$$

Both multiplicative terms in this last equation being negative, we then deduce that $G''(h) > 0$. Furthermore, noticing in the expression of the function $G(h)$ that:

$$G(h) = 2h + \underbrace{\tau(p_0, h)[p_i^n - p_0]}_{<0} + \underbrace{\tau_i^n[p_i^n - p_0] - 2h_i^n}_{<0}, \quad (78)$$

and knowing that in a shock wave, $0 < \tau(p_0, h) < \tau_i^n$, it is then possible to write :

$$\left\{ \begin{array}{l} \lim_{h \rightarrow \infty} G(h) = +\infty, \\ \lim_{h \rightarrow 0} G(h) < 0. \end{array} \right. \quad (79)$$

In the expression (76) of the first derivative of $G(h)$, $\frac{\partial \tau}{\partial h}(p_0, h)$ is positive and $(p_i^n - p_0)$ is negative so that $G'(h)$ has a unique zero \bar{h} in $] -\infty, +\infty[$ implicitly defined by $\frac{\partial \tau}{\partial h}(p_0, \bar{h}) = -\frac{p_i^n - p_0}{2} > 0$. This zero can be either positive or negative and two cases have to be considered.

First case $\bar{h} > 0$:

In this case, the zero of $G'(h)$ is in the interval of interest $]0, +\infty[$. We then deduce from the sign of $G''(h)$ that $G'(h)$ is an increasing function in $]0, +\infty[$ and that $G(h)$ is a decreasing function in $]0, \bar{h}]$ and an increasing function in $[\bar{h}, +\infty[$. The relations (79) thus lead to the conclusion that there exists a unique zero of $G(h)$ in $[\bar{h}, +\infty[$.

Second case $\bar{h} < 0$:

In this case, the zero of $G'(h)$ is not in the interval of interest $]0, +\infty[$. We then deduce from the sign of $G''(h)$ that $G'(h)$ is an increasing function in $]0, +\infty[$ and that $G(h)$ is an increasing function in $]0, +\infty[$. The relations (79) thus lead to the conclusion that there exists a unique zero of $G(h)$ in $]0, +\infty[$.

Appendix 4: Results for the contact discontinuity double expansion wave and double shock wave cases

Contact discontinuity

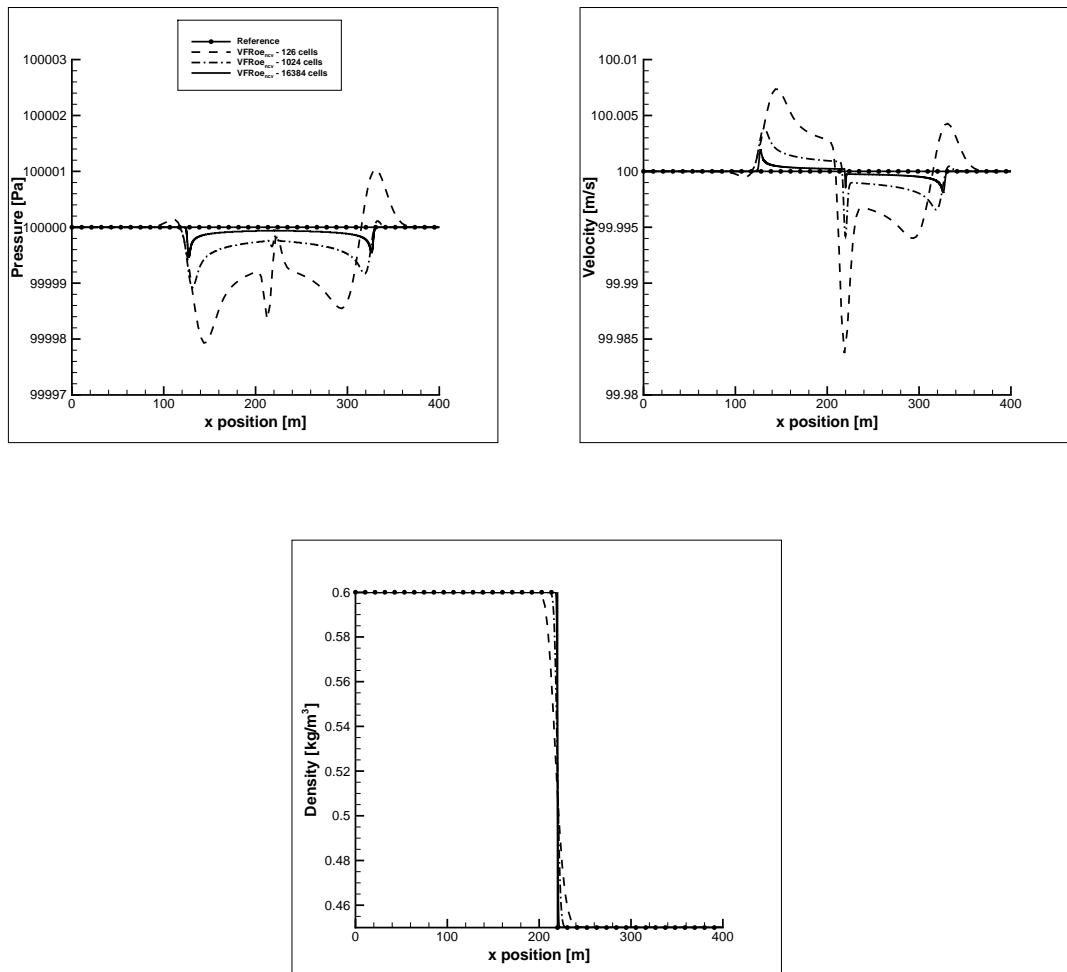


Figure 23: Comparison of pressure, velocity, and density profiles to the analytical solution for a contact discontinuity using VFRoe and the tabulated IAPWS EOS

Double expansion wave

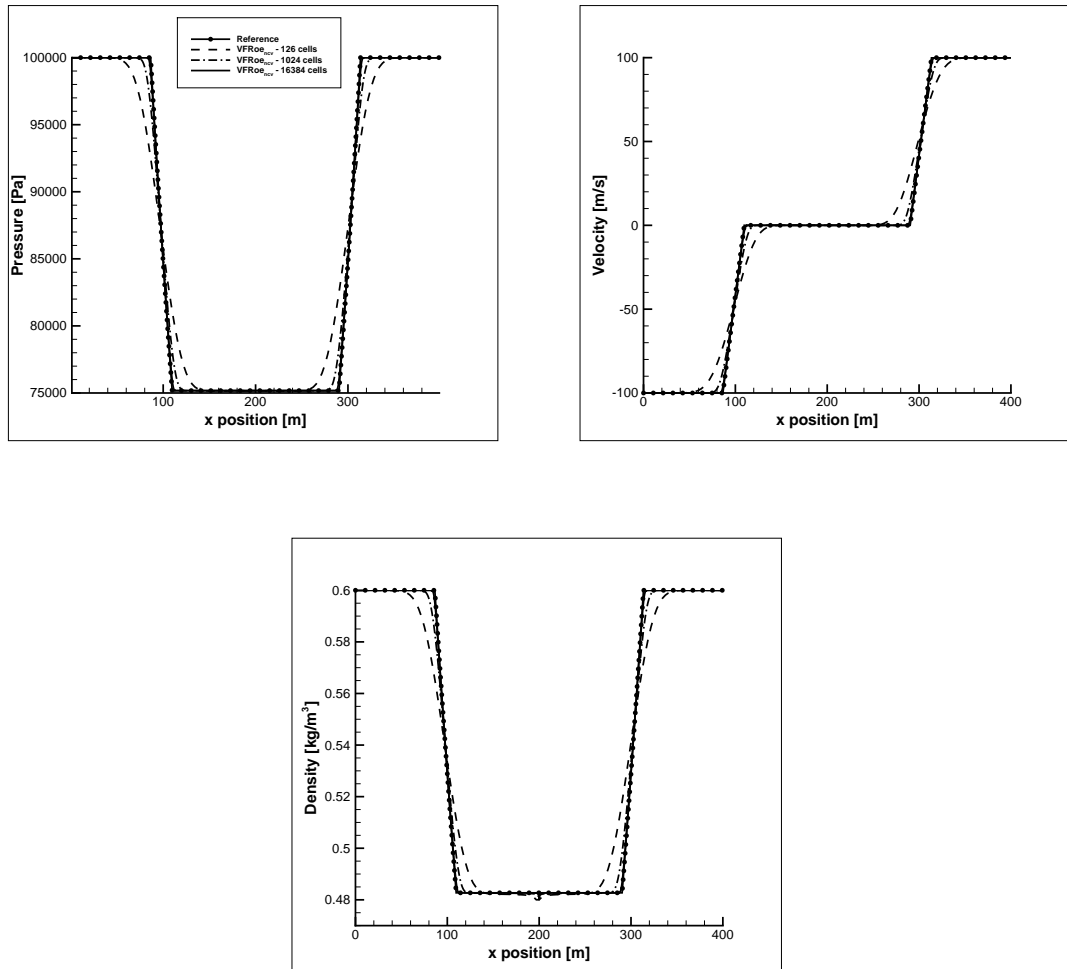


Figure 24: Comparison of pressure, velocity, and density profiles to the analytical solution for a double symmetric expansion wave using VFRoe and the tabulated IAPWS EOS

Double shock wave

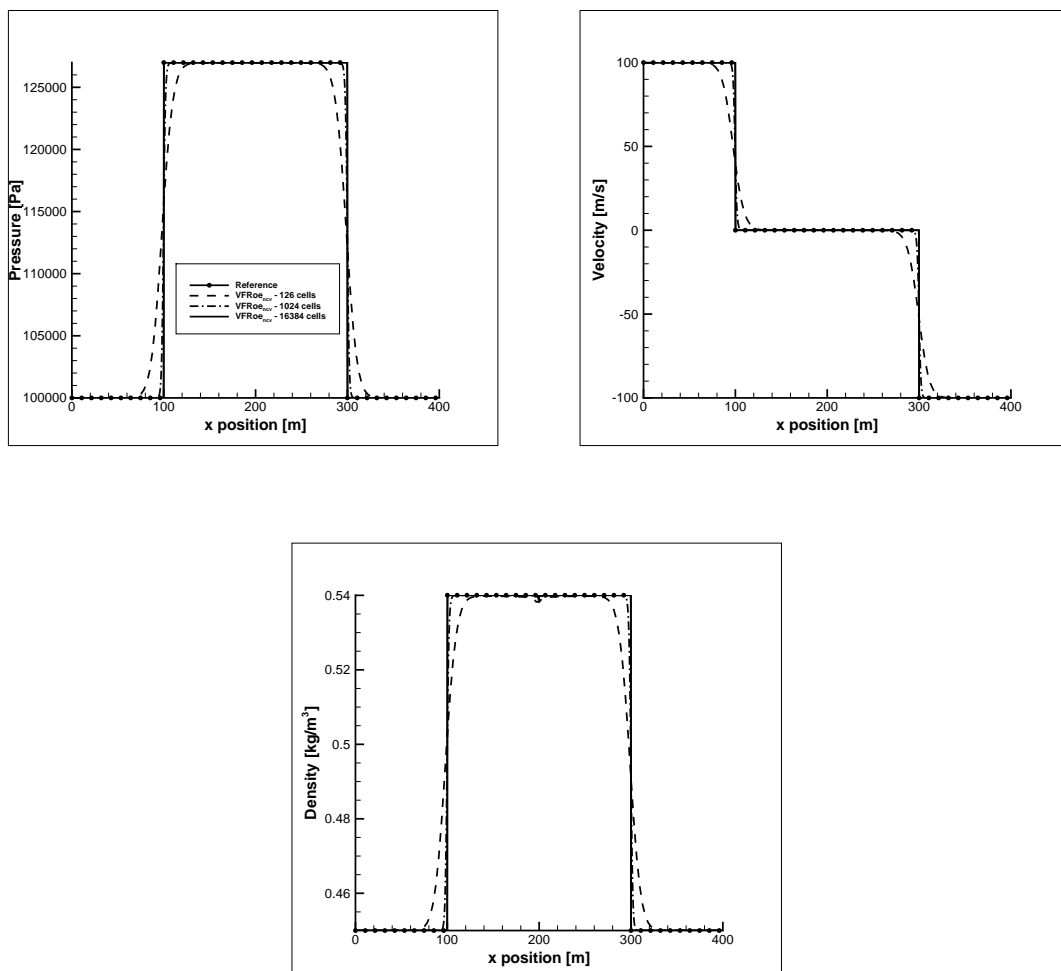


Figure 25: Comparison of pressure, velocity, and density profiles to the analytical solution for a double symmetric shock wave using VFRoe and the tabulated IAPWS EOS

Appendix 5: Exact solution of the Riemann problem - Application to the IAPWS EOS

The fundamental equations for the solution of the exact Riemann problem have been studied by many authors, with applications to real gases (see [Smoller 83] or [Godlewski 96] for example). The application to the IAPWS EOS is not straightforward as it does require many inversions. Relations for each wave are reminded below [Smoller 83], [Godlewski 96].

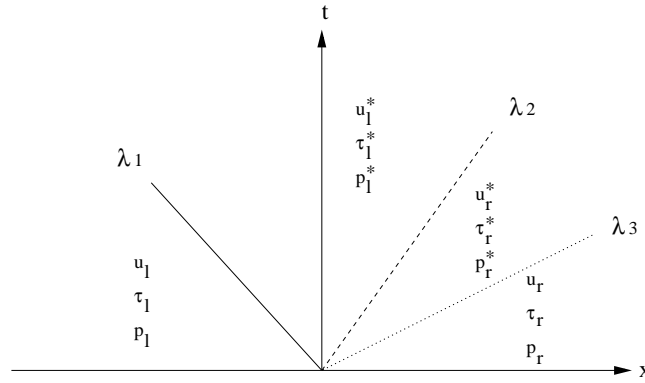


Figure 26: Riemann problem for the Euler equations

A sketch of the solution of the Riemann problem for the Euler equations is reminded on Fig. 26. The solution consists in four states separated by three waves. The two extreme waves are associated with genuinely non linear fields (shock waves or expansion waves) and the intermediate wave with a linearly degenerate field (contact discontinuity). Using the notation " α " for left and right states, and "*" for the intermediate state (Fig. 26), the unknowns of the Riemann problem are $(\tau_l^*, \tau_r^*, u^*, p^*)$ with $\tau = \rho^{-1}$ the specific volume, and the relations given below are used across contact discontinuity, shock waves and expansion waves.

Contact discontinuity

$$\begin{cases} u_l^* = u_r^* = u^*, \\ p_l^* = p_r^* = p^*. \end{cases} \quad (80)$$

Expansion wave

$$s(p_\alpha, \tau_\alpha) = s(p^*, \tau_\alpha^*), \quad (81)$$

$$u^* = u_\alpha \pm \int_{\tau_\alpha}^{\tau_\alpha^*} \frac{c(s_\alpha, \tau')}{\tau'} d\tau'. \quad (82)$$

A trapezoidal method is used to evaluate the integral in the relation (82), after setting the correct sign before the integral with the positive (respectively negative)

sign in the 1-wave (respectively the 3-wave). Using the IAPWS, speed of sound is given by $c_\alpha^* = c_{iapws}(p^*, T_\alpha^*)$, p^* and T_α^* being unknown at this calculation step. The temperature T_α can be evaluated with a Newton-Raphson technique, using the polynomial relation $\tau_\alpha = \tau_{iapws}(p_\alpha, T_\alpha)$, τ_α and p_α being known. Then, the entropy conservation is used to compute $s_\alpha = s_\alpha^* = s_{iapws}(p_\alpha, T(p_\alpha, \tau_\alpha))$. At this time, s_α , τ_α and τ_α^* are known (τ_α^* from previous iteration), and p^* , T_α^* are still unknown. With two unknowns and two equations ($s_\alpha^* = s_\alpha = s_{iapws}(p^*, T_\alpha^*)$ and $\tau_\alpha^* = \tau_{iapws}(p^*, T_\alpha^*)$), the problem is closed. Then, the polynomial expression for the speed of sound is used, and the integral can be evaluated using a trapezoidal method. Finally, a new evaluation of τ_α^* is performed using $\tau_\alpha^* = \tau_{iapws}(p^*, T_\alpha^*)$

Shock wave

$$\begin{cases} e_\alpha^*(p^*, \tau_\alpha^*) - e_\alpha(p_\alpha, \tau_\alpha) + \frac{1}{2} (p_\alpha + p^*) (\tau_\alpha^* - \tau_\alpha) = 0, \\ M = \frac{u^* - u_\alpha}{\tau_\alpha^* - \tau_\alpha}, \\ M^2 = -\frac{p^* - p_\alpha}{\tau_\alpha^* - \tau_\alpha}, \end{cases} \quad (83)$$

with:

$$\begin{cases} \tau_\alpha^* < \tau_\alpha, \\ p^* > p_\alpha, \\ u^* - u_\alpha < 0 \text{ for a 1-wave,} \\ u^* - u_\alpha > 0 \text{ for a 3-wave.} \end{cases} \quad (84)$$

In the case of a shock wave, the flow is compressed and the pressure rises, so that $(p^* - p_\alpha)$ is strictly positive and $(\tau_\alpha^* - \tau_\alpha)$ is strictly negative. Thus, a negative sign appears on the last equation in (83). Across the waves, τ_α , p_α are known and τ_α^* is given by the last iteration. A Newton-Raphson method is used to solve $e_\alpha^*(p^*, \tau_\alpha^*) - e_\alpha(p_\alpha, \tau_\alpha) + \frac{1}{2} (p_\alpha + p^*) (\tau_\alpha^* - \tau_\alpha) = 0$. First, $e_\alpha(p_\alpha, \tau_\alpha)$ is computed using the polynomial expression for $e_{iapws}(p, T)$. As the temperature is unknown, an inversion is mandatory. A second polynomial expression is used $\tau_{iapws}(p, T)$ and $e_\alpha^*(p^*, \tau_\alpha^*)$ can be computed. Then the zero of the function can be evaluated, still using the Newton-Raphson inversion technique for $e_\alpha(p_\alpha, \tau_\alpha)$. The pressure p^* being known, the velocity computation is straightforward: $u^* = u_\alpha - \frac{M}{|M|} \sqrt{-(p^* - p_\alpha)(\tau_\alpha^* - \tau_\alpha)}$ (with $(p^* - p_\alpha)$ positive and $(\tau_\alpha^* - \tau_\alpha)$ negative, a negative sign appears under the square root). The evaluation of the density is performed using $\tau_\alpha^* = \tau_{iapws}(p^*, T_\alpha^*)$.

Resolution method

The relations across each kind of waves being known, the method used to solve the exact Riemann problem is the following:

- The problem is initialized using $\tau_\alpha^* = \tau_\alpha$.

- A test is performed on specific volumes:
 - Case 1: if $\tau_\alpha^* \geq \tau_\alpha$, the wave is an expansion wave, Riemann invariants relations are used.
 - Case 2: if $\tau_\alpha^* < \tau_\alpha$, the wave is a shock wave, Rankine-Hugoniot relations are used.
- τ_l^* and τ_r^* are calculated on each side using the appropriate relations (Case 1 or Case 2).
- A Newton-Raphson is used to solve the contact discontinuity relations (80), until convergence (absolute difference fixed to 1×10^{-8} for the unknown, $|u_l^* - u_r^*|$ and $|p_l^* - p_r^*|$).